

CHARACTERIZING POROSITY FOR 3D PRINTED
HYDROXYAPATITE SCAFFOLDS OF VARYING
DENSITY AND COMPOSITION

By

DAVID G. JENKINS

Bachelor of Science in Geology

Texas A&M University

College Station, Texas

2014

Submitted to the Faculty of the
Graduate College of the
Oklahoma State University
in partial fulfillment of
the requirements for
the Degree of
MASTER OF SCIENCE
December, 2022

CHARACTERIZING POROSITY FOR 3D PRINTED
HYDROXYAPATITE SCAFFOLDS OF VARYING
DENSITY AND COMPOSITION

Thesis Approved:

Dr. James Smay

Thesis Adviser

Dr. Pankaj Sarin

Dr. Jake Bair

ACKNOWLEDGEMENTS

First and foremost, I would like to thank Dr. Smay for his instrumental guidance throughout the entirety of my research. He was always available for conversations that not only dove into avenues of science previously unknown to me but, helped me realize my potential along the way. Also, I am grateful for Dr. Sarin and Dr. Bair being on my committee.

I would like to thank Dr. Kim for lending me his time and expertise while analyzing samples on the scanning electron microscope.

I would like to thank Siddhesh Chaudhari for performing thermal analyses of my samples in addition to many conversations in the lab on how to enhance my research. Likewise, Rohit Bukka helped characterize my samples using Mercury Intrusion Porosimetry and provided many helpful pointers for porosity analysis.

Most importantly, I could not have done this without the love and support from my amazing girlfriend Jenny Nguyen and my family. Even though she was in a different city, Jenny was with me every step of the way over the last two years. She was my calm, steady source of wisdom, always reminding me to find joy in the mundane and that obstacles are meant to be overcome. I will be forever grateful—this achievement is hers as well as mine. Also, my mother (Dena Jenkins), brother (Danny Jenkins), sister (Jennifer Moore) and brother-in-law (Andrew Moore) were there to celebrate the victories and strategize when obstacles made things difficult. I owe my success to them. Lastly, my dad, Dr. Daniel Jenkins, set me on this path many years ago as a child, when

he encouraged curiosity and helped me find my love for the outdoors. Because of this, I found a deep respect and reverence for nature and began seeing it as a source of knowledge and inspiration for design. Even though he is no longer with us, I know he would be proud of how far I've come. I am blessed to have had a father like him. Thank you, Dad.

Name: DAVID G. JENKINS

Date of Degree: DECEMBER, 2022

Title of Study: CHARACTERIZING POROSITY FOR 3D PRINTED

HYDROXYAPATITE SCAFFOLDS OF VARYING DENSITY AND COMPOSITION

Major Field: MATERIALS SCIENCE AND ENGINEERING

Abstract: Recent advances in materials science and tissue engineering give the ability to create three-dimensional biocompatible ceramic scaffolds for bone repair. Applications include a variety of bone defects such as non-unions, replacing bone loss from trauma or disease, and maxillofacial reconstruction. An important, yet understudied, aspect of creating artificial bone requires knowledge of porosity. In this study, hydroxyapatite (HA) synthetic bone scaffolds were fabricated through an extrusion-based 3D printing technique called robocasting to characterize three modes of porosity distinguished by a range of pore diameter size: (i) ceramic pores (100nm – 2 μ m), (ii) intermediate pores (2 μ m – 70 μ m), and (iii) structural pores (>70 μ m). Highly porous scaffolds were designed with a CAD software and printed with an ‘ink’ composed of a stable suspension of colloidal HA and some contained a fugitive pore former of poly(methyl methacrylate) (PMMA) particles between 20 and 65 microns. Porosity was characterized in two ways: (i) pure HA scaffolds were printed and sintered at 1200°C (highest sintering temperature), 1175°C, and 1150°C and, (ii) composite scaffolds were printed in HA/PMMA volumetric ratios of 95/5, 85/15, 75/25, 60/40, and 50/50 and were each sintered at 1200°C. As intuition would assume, the HA scaffolds showed a decrease in porosity as sintering temperature was increased and the HA/PMMA scaffolds showed an increase in porosity as the fugitive pore former volume fraction was increased. From this work, a method is established for creating a range of ceramic porosities due to sintering temperature, a range of intermediate porosities due to the volume fraction of fugitive pore former, and the ability to control structural porosity through CAD (this was only shown through the two scaffold models used and was not the focus of this study).

TABLE OF CONTENTS

Chapters	Page
I. INTRODUCTION.....	1
1.1 Objectives.....	1
1.2 Motivation.....	1
1.3 Application.....	2
1.3.1 Dentistry.....	2
1.3.2 Maxillofacial Reconstruction.....	3
1.3.3 Non-Unions.....	3
1.4 Background.....	4
1.4.1 Bone Structure.....	4
1.4.2 Biocompatibility.....	5
1.4.3 Direct Ink Writing.....	7
1.4.4 Colloidal Processing.....	11
II. MATERIALS AND METHODS.....	15
2.1 Ceramic Processing.....	15
2.2 Ink Formulation.....	16
2.3 RoboCAD.....	20
2.4 Robocasting.....	21
2.5 Solvent Leaching.....	29
2.6 Sintering.....	30
2.7 Archimedes Method.....	32
2.8 Backscattered Electron Imaging.....	35
III. RESULTS.....	37
3.1 Helium Pycnometry.....	37
3.2 Thermal Analysis for PMMA.....	37
3.3 Archimedes Density Testing.....	39
3.4 Mercury Intrusion Porosimetry.....	42
3.5 Scanning Electron Microscopy.....	47
3.6 Backscattered Electron Imaging.....	48
3.7 ImageJ Pore Size Analysis.....	50
3.8 Failed Experiments.....	51

Chapter	Page
IV. DISCUSSION.....	53
4.1 Archimedes Method.....	53
4.2 MIP.....	53
4.3 BSE.....	54
4.4 Ink Formulation	55
4.5 Future Work.....	55
V. CONCLUSION.....	57
REFERENCES	58
VITA.....	61

LIST OF TABLES

Table	Page
Table 1: Calculating the masses of the constituent ingredients for ink formulation	19
Table 2: Calculating HA and PMMA mass for ink formulation at each ratio	19
Table 3: Relevant data from the Archimedes method.....	39
Table 4: Data acquired from MIP	42
Table 5: BSE results for HA scaffolds.....	48
Table 6: BSE results for HA/PMMA scaffolds	49
Table 7: Pore size Analysis Data performed by ImageJ	51

LIST OF FIGURES

Figure	Page
Figure 1: Cortical bone vs. Trabecular bone.....	5
Figure 2: Direct Ink Writing Techniques. a) continuous filament writing and b) droplet-based writing.....	9
Figure 3: Illustration of the DLVO Theory showing particle attraction as a function of distance.....	13
Figure 4: Overview of basic types of rheological behavior	14
Figure 5: Hydroxyapatite powder a) before and b) after the calcination process	16
Figure 6: A Thinky cup showing a final ink passing the spatula test and displaying proper viscoelastic behavior	18
Figure 7: CAD models used for a) the HA/PMMA scaffold and b) the HA scaffolds.....	21
Figure 8: The robocasting printer in the Smay Lab	23
Figure 9: Constituent parts of the ink syringe assembly: a) the nozzle assembly, b) the tube and c) the ink syringe assembly	24
Figure 10: Ink syringe and nozzle fully assembled: a) the nozzle, b) the tube and c) the syringe	25
Figure 11: Robocasting nozzles: a) Red tip with a 250 μm diameter nozzle and b) Blue tip with a 410 μm diameter nozzle.....	26
Figure 12: Ink Syringe and Nozzle mounted and secured in the robocast printer.....	27
Figure 13: Robocasting in action (nozzle shown has a 250 μm tip diameter).....	28
Figure 14: RoboCad models from Figure 6 fabricated with Robocasting: a) HA/PMMA Scaffold from a 410 μm tip and b) HA Scaffold from a 250 μm tip	28
Figure 15: 85/15 HA/PMMA Scaffolds after the leaching process. Note the plastic film covering some of the scaffold voids	30
Figure 16: Sintering profiles for HA and HA/PMMA scaffolds	31
Figure 17: HA Scaffolds with same original dimensions showing varying amounts of densification due to sintering temperature: a) 1200°C, b) 1175°C and c) 1150°C.....	32
Figure 18: Mettler Toledo Density Kit for Archimedes analysis. Note the submerged scaffold for obtaining $m_{\text{submerged}}$	34
Figure 19: TGA curve for Transoptic PMMA powder.....	38
Figure 20: DSC curve for Transoptic PMMA powder	38
Figure 21: Ceramic rod porosity of HA scaffolds determined by Archimedes testing.....	40
Figure 22: Total porosity of HA scaffolds determined by volumetric analysis.....	40
Figure 23: Ceramic rod porosity of HA/PMMA scaffolds determined by the Archimedes method.....	41
Figure 24: Total Porosity of HA/PMMA scaffolds determined by volumetric analysis.	41
Figure 25: Bimodal pore size distribution for the HA scaffolds determined by MIP.....	43

Figure	Page
Figure 26: Distribution of pore sizes as pore former content is increased during MIP. Note the vertical lines marking the average intermediate pore diameter from BSE....	44
Figure 27: MIP Porosity variation due sintering temperature	45
Figure 28: MIP densities variation due to sintering temperature.....	45
Figure 29: MIP Porosity variation due to pore former content.....	46
Figure 30: MIP densities variation due to pore former content	46
Figure 31: SEM image of Transoptic PMMA	47

CHAPTER I

INTRODUCTION

1.1 Objectives

The objectives of this study are to: (1) establish a clear method for robocasting scaffolds of known porosity, (2) show a range of porosity variation through sintering, (3) show a range of porosity through fugitive polymer spheres, and (4) establish the threshold volume fraction of fugitive polymer spheres required to form a percolating network.

1.2 Motivation

Advances in additive manufacturing have shown potential in the field of tissue engineering.[1] From bones to organs to specific tissue membranes, additive manufacturing can create a wide range of tissues for a myriad of applications.[2] However, the most promising avenue of tissue engineering is found in fabrication of synthetic bone scaffolds for various bone defect repair and many fabrication techniques are being tested.[3-7] Globally in 2019 there were 178 million new bone fractures and 455 million people dealing with long term effects of a bone fracture.[8] Additionally, long health and poor diets have led to a rise in bone defect comorbidities like osteoporosis and type 2 diabetes, globally affecting 200 million 457 million persons, respectively.[9] The need for patient specific, tailorable solutions to bone defects is

growing each year. Merging the power of computer aided design, CAD, with modern materials science has yielded the ability to 3D print customized ceramic scaffolds of complex geometry with tissue compatibility.[10-12] Scaffold efficacy in a living body relies on several factors: biocompatibility, strength, and porosity among others. Bone scaffolds are currently the subject of extensive research and already have a limited role in surgical operations.[13] Additional research is required for more extensive utilization in the medical field. This study focuses on contributing porosity characterization of scaffolds to the literature.

1.3 Application

1.3.1 Dentistry

Bone grafts are already used in the dental industry. Oral decay leads to loss of bone mass and structure in teeth and the jaw. Often, dental repairs are not possible when too much tissue in the teeth and jaw have decayed to a point of instability or are missing entirely. For jaws, bone grafts can be used to stabilize the bone and create a sufficient platform for tooth implants. Synthetic scaffolds could replace bone grafts in these applications.[14] However, teeth can't be corrected with grafts, leading to a wide array of solutions. The current method attempts to reflect the natural structure by using an artificial implant composed of a titanium root and ceramic tooth. These processes are expensive and often use materials that are foreign to the body like titanium. 3D printing teeth shows promise of an all-ceramic tooth replacement.[15] Conventional methods require scaffolds and tooth replacements be made in different ways due to a large disparity in porosity. 3D printing scaffolds and teeth using biocompatible ceramics with porosity control shows promise at a lower price in the dental industry.

1.3.2 *Maxillofacial Reconstruction*

Like dental applications, bone scaffolds are now being considered a viable option for mandible (lower jaw) repair and even replacement.[16] Events such as trauma from car wrecks, cancer, advanced gum disease can result in a partial or complete removal of the mandible. Across the population there is a high diversity in size and shape of the mandible, meaning an adequate inventory of premade artificial mandibles would be difficult to maintain and use effectively in the hospital setting. Possibly, a more effective method would be to fabricate a synthetic scaffold based on imagery of the patient's mandible. Custom size and shape of bone scaffolds from CAD allows the creation of a patient specific jaw replacement with host tissue compatible porosity.

1.3.3 *Non-Unions*

Non-unions present an acute need for a tailorable, highly porous bone scaffold and is the application focused on in this study. A non-union is a bone defect occurring after a fracture where the bone interfaces at a fracture location struggle to rejoin and heal. Many factors can contribute or lead to this phenomenon, including diabetes, smoking, certain medications, fracture configuration, bone density, and degree of immobilization among others. Patients with a non-union experience high morbidity, elevated long-term pain, lack of mobility, lowered quality of life, expensive medical bills, and often a shortened life span. Non-unions typically occur in the long bones of the body with the highest prevalence occurring in the tibia and clavicle. The best treatment for these persistent injuries is a bone graft surgery, where the graft is taken from the patient's hip and is secured in the target area with bone putty, which needs to be removed 6 weeks later.

Additionally, metal plates and screws are used to provide mechanical structure and bear the load during healing. Unfortunately, this intensive procedure, which requires multiple surgeries in two locations, has less than a 70% success rate. For the cases that failed the procedure must be repeated, potentially taking years to heal or never for some. With approximately 9 million non-unions occurring worldwide each year, there is a demand for 3D printed bone scaffolds with tailorable porosity. Scaffolds designed for this application are the focus of this research.[17, 18]

1.4 Background

1.4.1 Bone Structure

Creating a viable porous synthetic scaffold for surgical bone repair requires some knowledge of bone structure. The bones throughout the human body range significantly in size and shape, but importantly every bone has two specific types of tissue in common. The solid outer portion of bones are called cortical, or compact, bone and are characterized by high density and low amounts of porosity. Comprising 80% of the overall skeletal mass, the cortical bone functions as a solid outer case and provides the structural strength of bone. Beneath the cortical bone and occupying the interior lies the second main bone tissue type: trabecular bone. Also called cancellous or spongy bone, this tissue makes up 20% of the skeletal mass and is characterized by low density and high amounts of porosity ranging from 75-95%. Trabecular bone has upwards of ten times the surface/volume ratio of cortical bone and serves an interconnected network providing space for bone cells, red blood cells, nerves, blood vessels, and bone marrow to operate and carry out essential functions of the body. Since trabecular bone tissue is the medium in which nutrients and bone cells flow towards a bone defect and serves as the

interface where the healing process begins, this highly porous spongy tissue is the target structure to emulate when designing synthetic scaffolds. [19]

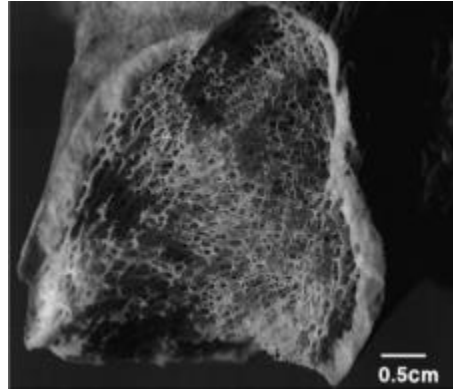


Figure 1: Cortical bone vs. Trabecular bone. [20]

1.4.2 *Biocompatibility*

A synthetic bone scaffold's success, or biocompatibility, will be discussed in two ways: (i) composition and (ii) porosity. Compositional effects on biocompatibility have already been characterized and are not the focus of this paper. However, it is important to discuss because it allows the focus to be on the characterization of porosity.

Biocompatibility in tissue engineering is defined as the ability for a non-native material to improve or restore a function of the host and, ultimately, be incorporated by the host. Inclusion by the host is a relatively simple process if the host tissue and the inorganic scaffold are composed of the same mineral composition and have similar structure.

Biocompatibility for synthetic bone scaffolds is perhaps the most important metric when evaluating success of a scaffold and is characterized by osteoinduction (new bone cell growth from undifferentiated cells), osteoconduction (new bone cell growth on a

particular surface), and osseointegration (bone growth from host tissue into the implanted structure). Combined, these three processes describe complete acceptance by the host.

Artificial scaffolds made of inorganic materials, including HA, are considered poor osteoinductors but cell proliferation can be enhanced by the inclusion of Bone Morphogenic Protein (BMP) in the scaffold.[21] The pore spaces in a scaffold can be filled or the surface area coated with BMP prior to surgical implementation to boost osteoinduction. The importance of porosity is worth noting here, but osteoinduction and BMP will not be discussed further as this behavior of the scaffolds *en vivo* is beyond the scope of this study.

Previous studies have found calcium phosphate in the form of HA is extremely osteoconductive and is frequently used for bone defects and in dental applications. Highly porous scaffolds composed of HA are desirable because they combine the high osteoconduction of HA with the elevated surface area in the structure. Also, trabecular tissue has porosity up to 95%, so maximizing the porosity in HA scaffolds should give similar osteoconductive properties to that of host tissue. This gives nutrients and bone cells a large area to travel throughout the scaffold and form bone tissue.

HA is highly biocompatible and the most stable form of tricalcium phosphate composing up to 70% of the human skeletal system by weight. HA exists naturally in abundance and can also be synthesized in laboratories as a ceramic species. By using HA ceramic powder as the building block material when fabricating scaffolds, high amounts of biocompatibility can be expected. However, HA alone has lower strength than other forms of calcium apatite, such as beta-tricalcium phosphate (β -TCP). β -TCP has higher

strength but has lower rates of osteoconduction. In applications where the scaffolds are surgically implanted in animals, a typical HA/ β -TCP ratio of 15/85 is used to promote both osteoconduction and strength. In this study, strength is of no concern and the focus is solely on porosity characterization, so scaffolds composed of pure HA are sufficient.[22]

The last metric of biocompatibility, osseointegration, is dependent on the porosity of the scaffold, assuming osteoinduction/conduction are occurring. In a typical bone fracture, the broken segments experience osseointegration across the trabecular interface where bone tissue growth spans the gap and fuses the two structures together. Recreating this affect in an interface between trabecular tissue and synthetic scaffold requires the scaffold to have similar porosity of trabecular tissue in the 75-95% range.

In conclusion, all three metrics of biocompatibility in artificial bone scaffolds are enhanced by maximizing porosity.

1.4.3 *Direct Ink Writing*

Additive manufacturing, or 3D printing, is the process of constructing three dimensional structures by depositing material layer by layer from a computer-aided design (CAD) file. Additive manufacturing dates to 1983 with the invention of a fabrication technique called stereolithography where a bath of photo-sensitive polymer resins are selectively cured by UV lasers to create three dimensional structures.[1] In recent decades dozens of additive manufacturing techniques have been developed capable of printing a wide range of materials including plastics, metals, ceramics, and more. Additive manufacturing, regardless of the type, has many pros and cons. Some of the

advantages today include inexpensive rapid prototyping processes, customized parts, minimal waste material, reduction in assembly steps, capable of complex geometries, and range of materials. Disadvantages include expensive machines, slow speed for mass production, and high price per part for mass production. [23]

Additive manufacturing is ideal for fabricating artificial bone scaffolds because of three previously mentioned advantages: (i) ceramic capability, (ii) complex geometries, (iii) and customization. The ability to manufacture ceramics by 3D printing offers some advantages over other ceramic manufacturing methods. Conventional ceramic processing techniques largely focus on creating parts with high density and require green state particle compaction before sintering. Compaction can be achieved several ways, but this step eliminates the possibility of creating an intricate shape with internal structure like a scaffold. Many applications of ceramics require post processing of the sintered sample before being ready for its intended use. Due to the extremely hard and brittle nature of sintered ceramics, this is a tedious and expensive step, often resulting in failure if not done correctly. Since the goal of a ceramic scaffold is high porosity, a method like 3D printing can be chosen that allows complex geometry, does not require a compaction step, and requires no post processing. Furthermore, conventional ceramic techniques require molds or dies to shape the ceramic particles into the desired green state geometry. These molds are expensive and require time to manufacture, limiting the ability of conventional methods to create unique ceramic shapes in a timely, cost-effective manner. Conversely, additive manufacturing allows the creation of custom parts from a CAD file in a quick, inexpensive method.[24]

Synthetic bone scaffolds are fabricated through an extrusion-based technique of additive manufacturing called Direct Ink Writing (DIW) or Robocasting. Direct Ink Writing is the more common title for this extrusion technique, but Robocasting is used when discussing the specific ceramic scaffold fabrication in the Smay lab. There are two main types of DIW: continuous filament-based writing and droplet-based writing. These are shown in Figure 2.[25]

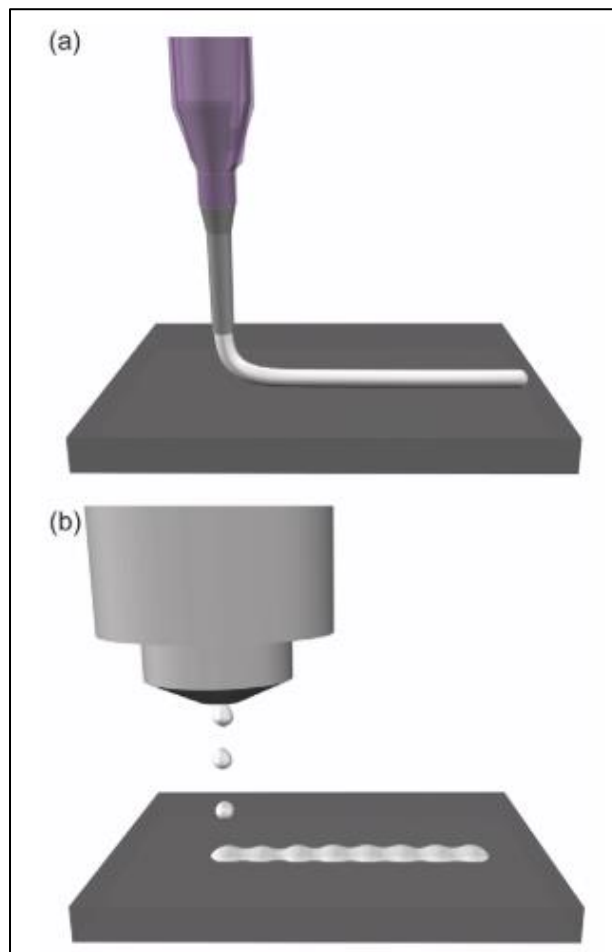


Figure 2: Direct Ink Writing Techniques. a) continuous filament writing and b) droplet-based writing. [25]

Filament based writing can be performed in two ways: (i) constant displacement and (ii) constant pressure. The printer used in this study is of the constant displacement filament-based configuration. In this method a viscous liquid-based particle suspension exhibiting pseudoplastic behavior flows through a narrow nozzle at controlled deposition rates to achieve a filament with constant diameter. Achieving constant diameter filaments requires a syncing of the volumetric flow rate through mechanical suppression of the plunger in the ink reservoir and the lateral rate of motion of the nozzle in the x-y plane. The extruded filament has a rigid core with a fluidic surface allowing shape retention and fusing of filaments at contact points. Structures are formed by moving the nozzle in the x-y plane during deposition following a predetermined tool path created by CAD software. When a layer is complete, the nozzle is moved a predetermined distance vertically, based on nozzle tip diameter, in the z-direction and the process continues until completion. [26, 27]

The DIW process follows a consistent set of steps to produce a highly sintered, porous ceramic scaffold. The process begins with the digital creation of the desired structure in a CAD software program in the form of an .stl file. Next, the .stl file is modified by a slicer software, which takes the three-dimensional object and slices it into a stack of horizontal layers. The slicer then analyzes the layers and generates a .gcode file containing layer specific tool pathways for the nozzle to trace and other directions for creating the final structure. Next, a ceramic paste is mixed and loaded into the printer. The .gcode is executed and prints the structure layer by layer. The structure is left out in air to dry completely before placing in furnace for the sintering process. [25, 28]

1.4.4 *Colloidal Processing*

Using filament based DIW for synthetic scaffold fabrication requires precise ink formulation. The ink must flow smoothly during extrusion and become rigid upon exiting the nozzle for shape retention. This is achieved with by controlling several critical factors: (i) contains a controlled solids volume fraction, (ii) exists as a flocculated colloidal suspension, (iii) exhibits appropriate viscoelastic behavior.

Solids volume fraction describes the ratio of solid particles to the liquid medium in a heterogeneous solution. When formulating concentrated colloidal inks, the solids fraction should be maximized to avoid cracking and shrinkage while drying. However, high volume fractions allow rapid drying of the ink and potential clogs at the nozzle exit. This is prevented by writing onto a substrate submerged in an oil bath. The theoretical maximum volume fraction for densely packed spherical particles is 0.74. In this case the liquid phase only occupies the interstitial pore spaces, and a dilatant rheology would dominate. However, too little solids in solution allows the Newtonian rheologic behavior of the liquid phase to dominate and flow too freely. Smay et al. showed a solids volume fraction of 0.47 for colloidal inks creates a rheology between dilatant and Newtonian that will be discussed further. [29]

Colloids are particles having at least one dimension in the size range of 10^{-3} to 1 μm . Colloidal suspensions are a heterogeneous solution of colloid particles in a liquid medium. During filament based DIW, a concentrated colloidal ink, or gel, is extruded as a rod onto the substrate. The ink must be able to flow out of the nozzle as a paste and set instantly. This behavior occurs during extrusion when the outer shell of the filament is

stressed beyond the ink's yield stress and gives into shear flow, while the inner core retains elastic behavior and provides shape retention. The outer shell of the rods demonstrates shear memory and remains soft, allowing contact points between rods of subsequent layers to fuse together. The viscoelastic behavior of the ink can be described as pseudoplastic with yield stress rheology. When the extrudate is removed from the oil bath and allowed to dry, the solids volume fraction increases causing a shift from pseudoplastic to dilatant rheology. Understanding how a simple colloidal suspension of ceramic particles in water can have such a finely tuned viscoelastic behavior requires knowledge of colloidal processing.[30]

Achieving appropriate viscoelastic behavior in the ink is performed by manipulating the colloid surfaces by adsorption of a layered structure of various polymers and is demonstrated by the ink formulation process. The first step of colloidal ink formulation is adding 0.47 colloidal ceramic volume fraction to distilled water. The colloids at this point are not well dispersed and the solution exhibits Newtonian fluid behavior. The particles are not well dispersed due to attractive electrostatic forces, causing reversible aggregation. This behavior is due to phenomenon described by the DLVO theory, where long-range Van der Waals forces attract particles, but a strong short-range electrostatic repulsion keeps particles from irreversible aggregation.[31]

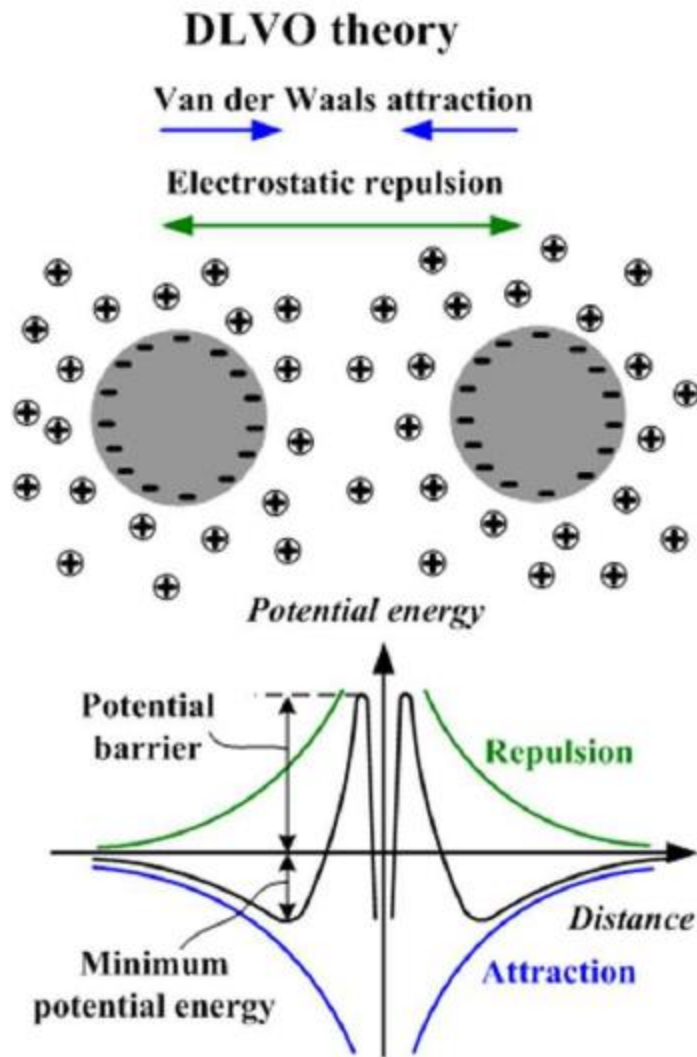


Figure 3: Illustration of the DLVO Theory showing particle attraction as a function of distance.

Adding a polymeric surfactant to the solution reduces the surface energies of the colloids and they dissociate into a complete dispersion. The solution has low viscosity, and the colloids can freely move throughout the solution. Viscosity is increased by inclusion of a viscosifier into the solution. This does not cause any attraction between particles, but the adsorption of the viscosifier on to the colloid surfaces increases their

diameter and reduces colloids' ability to slide past each other. The last step is the addition of a flocculant into the solution. The flocculant creates an attractive force between particles and causes the formation of flocs. The colloidal flocs change the suspension from a viscous Newtonian fluid to a non-Newtonian pseudoplastic. The strength of the flocs is directly dependent on the amount of added flocculant and adding too much will cause a pseudoplastic to dilatant rheology transition. An ink dominated by a flocculated structure can be tailored to exhibit shear thinning behavior. The flocs allow elastic recovery at low stress but contain a yield stress where the flocs are broken and the ink flows. As previously mentioned, the ink undergoes both rheologic processes during extrusion. The ink in contact with the tubing induces a shear thinning flow while the interior ink maintains elastic recovery. By precisely controlling solids volume fraction and colloidal surface chemistry, colloidal inks exhibiting pseudoplastic rheology with a yield stress can be formulated.[28, 29, 32]

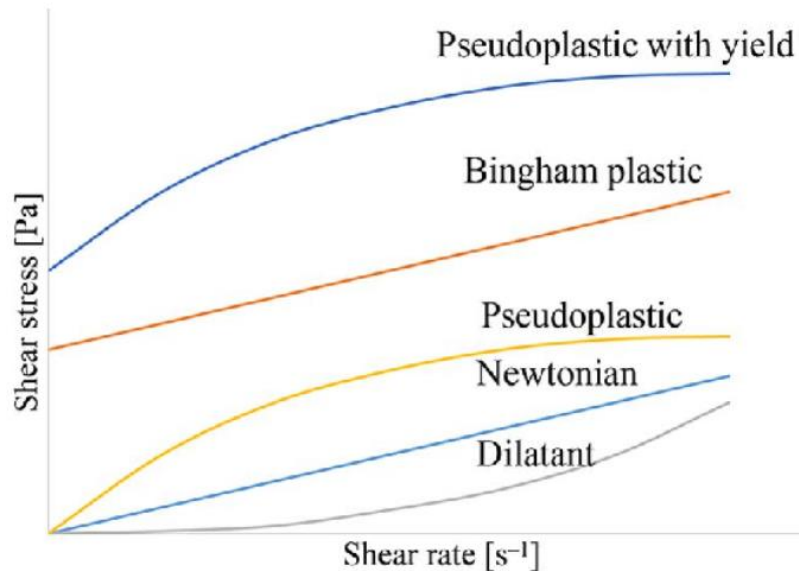


Figure 4: Overview of basic types of rheological behavior. [33]

CHAPTER II

MATERIALS AND METHODS

2.1 Ceramic Powder Processing

The primary constituent of the ceramic ink used in this study is a colloidal hydroxyapatite powder, $\text{Ca}_{10}(\text{PO}_4)_6(\text{OH})_2$, synthesized by Riedel-de-Haen labs in Germany. The raw powder has an average particle diameter of 2.78 μm . The ceramic powder needs to be processed before ink formulation to reduce particle surface area, i.e. make the particles more spherical, and increase particle size distribution. Spherical particles clog less, and high particle size distribution mitigates shrinkage effects during sintering by increasing packing density. The HA powder was calcined at 1100°C for 10 hours in a Lindberg Blue M furnace to reduce particle surface area. After cooling, the HA was milled in a Union Process attritor mill for 45 minutes at 70 rpm. The resulting suspension of HA particles in water was sieved to remove the milling media and placed in a StableTemp oven at 70°C for a day to remove all water. The HA was then placed in a 1-liter Nalgene bottle with large milling media and put in a paint shaker for 5 minutes to break up the chunks that formed during evaporation. The processed HA powder was measured using Helium pycnometry and found to have a density of $\rho_{\text{HA}} = 3.08 \text{ g/mL}$.

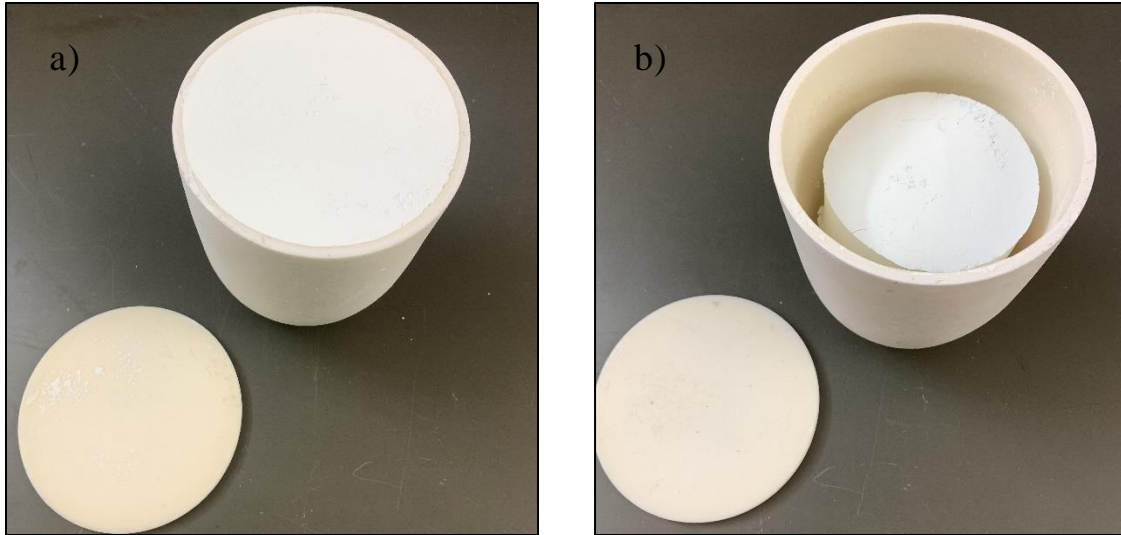


Figure 5: Hydroxyapatite powder a) before and b) after the calcination process.

2.2 Ink Formulation

The processed HA powder was used in the colloidal ink formulation. The ink for robocasting used in this study consists of highly concentrated suspensions of HA at a solids volume fraction (ϕ_{HA}) of $\phi_{HA} = 0.47$. Ink formulation begins with calculating the amount of all materials (equations 2.1-2. #) to be included based on the total desired volume of ink and solids volume fraction. Desired total volume (V_{Total}) of ink created in each batch is limited to by the size of the Thinky mixing cup, the Thinky AR-250 mixer (a viscous mixer), and a limited shelf life for optimal printing. For simplicity, a of $V_{Total} = 30$ mL was chosen as the target final volume. The DI water and about 30 g of zirconia milling media (just enough to cover the bottom of the Thinky cup with a single layer of milling media) were added to a Thinky cup with an ammonium polyacrylate dispersant (Darvan 821A) and swirled by hand several times until the brown-yellow color of D-

821A is no longer visible. D-821A is synthesized by R.T. Vanderbilt Company, Inc and available commercially at a 40% weight aqueous solution with a MW of 3,500. The measured amount of HA powder is then added to the Thinky cup and placed into the viscous mixer for 1 minute. After, the mixture is a stable dispersion of ceramic particles with a viscosity like 2% milk. To increase the viscosity, hydroxypropyl methylcellulose (Methocel F4M) is added to the suspension and mixed for 1 minute. F4M is a viscosifying agent and is synthesized by the DOW Chemical Company and is commercially available as a powder. A gel is made from the F4M powder at a 5% weight aqueous solution for use in the ink at a 7 mg/mL liquid concentration. After mixing the ink has a viscosity to that of whole milk. To gel the ink, polyethyleneimine (PEI) was added and mixed in 2 drop increments until the desired viscoelastic behavior is achieved. PEI is a flocculant and is synthesized by MP Biomedicals, LLC as a powder with a MW of 50,000-100,000. PEI for ink inclusion is prepared by making a 5% weight aqueous solution. Determining if the ink is ready for printing is determined by the spatula test, where a trench is dug through the ink and evaluated. If the trench is filled in or has rounded edges, more PEI is required. If the trench maintains sharp side walls, the ink is ready for robocasting, as shown in Fig. 6. Viscosity at this point falls between that of yogurt and peanut butter.

Some scaffolds contain a fugitive pore former for increasing final porosity. The pore former is Transoptic Powder composed of poly(methyl methacrylate) (PMMA) synthesized by Buehler and has spherical particles ranging in size from 20 μm to over 250 μm . To create a narrower particle size distribution, the powder was sieved to exclude all particles larger than 65 μm . The PMMA powder shares the total solids volume

fraction with the HA powder and was calculated at several HA/PMMA ratios (Table 2) of 95/5, 85/15, 75/25, 60/40, and 50/50. During ink formulation for scaffolds containing pore former, the HA and PMMA were added at the same step after D-821A and before F4M.

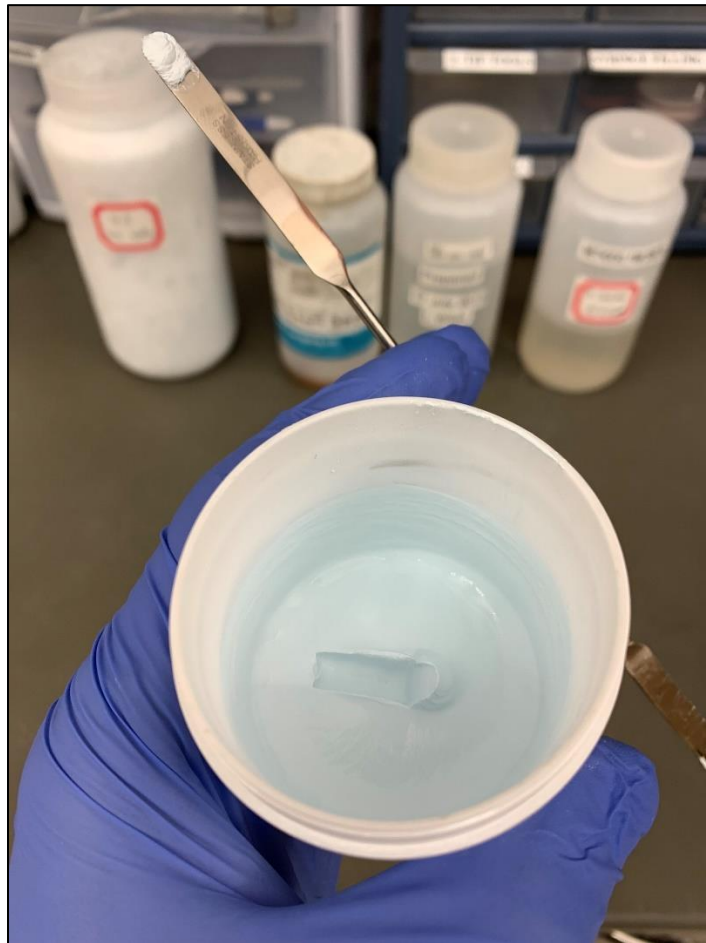


Figure 6: A Thinky cup showing a final ink passing the spatula test and displaying proper viscoelastic behavior.

Table 2: Calculating the masses of the constituent ingredients for ink formulation.

Inputs	Calculated
$V_{\text{Total}} = 30 \text{ mL}$	
$\Phi_{\text{HA}} = 0.47$	
$\rho_{\text{HA}} = 3.08 \text{ g/mL}$	
$V_{\text{HA}} = V_{\text{Total}} \cdot \Phi_{\text{HA}} = 14.1 \text{ mL}$	(1)
$m_{\text{HA}} = V_{\text{HA}} \cdot \rho_{\text{HA}} = 42.864 \text{ g}$	(2)
Dispersant Fraction (DF) = 0.0026	
821A Aq. Wt. Soln. ($\text{wt}_{821\text{A}}$) = 0.4	
$m_{821\text{A}} = (m_{\text{HA}} \cdot \text{DF}) / \text{wt}_{821\text{A}} = 0.279 \text{ g}$	(3)
$V_{\text{Liquid}} = V_{\text{Total}} - V_{\text{HA}} = 15.9 \text{ mL}$	(4)
F4M Aq. Wt. Soln. (wt_{F4M}) = 0.05	
$[\text{F4M}] = 7 \text{ mg/mL}$	
$m_{\text{F4M}} = ([\text{F4M}] \cdot V_{\text{Liquid}} \cdot 0.001) / \text{wt}_{\text{F4M}} = 2.23 \text{ g}$	(5)
$m_{\text{initial water}} = V_{\text{Liquid}} - m_{821\text{A}} - m_{\text{F4M}} = 13.391 \text{ g}$	(6)

Table 2: Calculating HA and PMMA mass for ink formulation at each ratio.

HA/PMMA		$V_{\text{Total}} = V_{\text{HA}} + V_{\text{PMMA}} \text{ (mL)}$		$m = \rho \cdot V \text{ (g)}$	
HA	PMMA	V_{HA}	V_{PMMA}	m_{HA}	m_{PMMA}
0.95	0.05	13.395	0.705	40.721	0.832
0.85	0.15	11.985	2.115	36.434	2.496
0.75	0.25	10.575	3.525	32.148	4.159
0.60	0.40	8.46	5.64	25.718	6.655
0.50	0.50	7.05	7.05	21.432	8.319

2.3 RoboCAD

Before 3D printing of any kind can occur, a printer needs a .gcode file containing exact details on the layer-by-layer steps required to fabricate an object. A .gcode file is produced by a slicer software, which is a 'sliced' model of a .stl file produced by CAD software. The robocasting printer in the Smay lab utilizes a CAD software called RoboCAD, which can make .stl and .gcode files through a single interface. RoboCAD was used to create 2 scaffold structures.

The HA scaffolds were designed to mimic a long bone cross section for a hypothetical non-union geometry, as shown in Fig. 7b. The scaffold is a short cylinder with a 20 mm diameter containing a hole in the middle with a diameter of 8 mm. The inner and outer walls were designed to be solid and mimic cortical bone, while the porous interior mimics trabecular bone. The inner circular void represents the medullary cavity. The scaffold consists of 16 layers alternating between radial and spiral patterns. The HA scaffolds were designed to be printed with a red tip (250 μm). RoboCAD software calculated each layer to be 196 μm tall when printed with a red tip.

The HA/PMMA scaffolds were designed to mimic generic bone graft geometry for bone defects, as shown in Fig. 7a. The scaffold is a simple 15 mm x 15 mm square, containing 16 layers of parallel rods that rotate 90° with each consecutive layer. The HA/PMMA were designed to be printed with a blue (410 μm) tip. RoboCAD software calculated each layer to be 320 μm tall when printed with a blue tip.

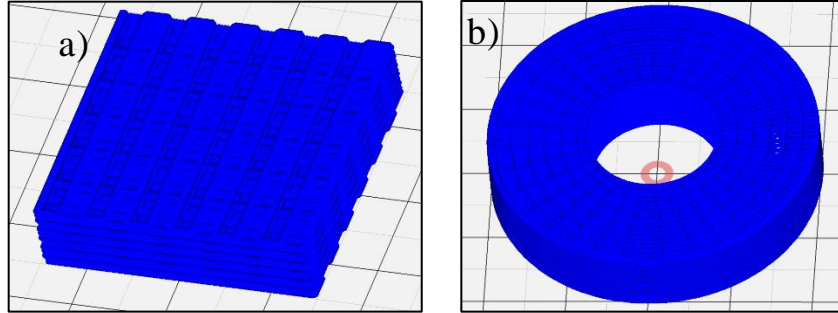


Figure 7: CAD models used for a) the HA/PMMA scaffold and b) the HA scaffolds.

2.4 Robocasting

The synthetic scaffolds were fabricated by the Robocasting printer in the Smay lab in the Helmerich Research Center, shown in Fig. 8. Prior to printing, the syringe must be loaded with ink and the syringe assembly, shown in Fig. 9, must be assembled. The Robocast printer is currently configured to extrude ink from a plastic 3 mL syringe reservoir. Filling this reservoir is a nuanced process focused minimizing the inclusion of air bubbles in the ink while being transferred from the Thinky cup to the 3 mL syringe. Eliminating bubbles entirely is impossible but can be minimized by using a plastic 10 mL staging syringe. The plunger from this syringe is removed and cut just below the rubber tip and a cap is placed over the nozzle. A spatula is used to carefully load the 10 mL syringe with ink from the Thinky cup one scoop at a time. This process must be done quickly due to the rapid drying kinetics of the ink. Once the syringe contains roughly 8 mL of ink, the rubber plunger tip is inserted into the 10 mL syringe until it is entirely in the syringe, leaving a small gap of air at the top. The 10 mL is oriented vertically with the plunger end down and subjected to mechanical excitation to allow air bubbles to flow through the suspension to the top surface of the ink. When there is no more bubble

motion, the plunger is pushed to remove the air bubble, leaving a syringe of ink with minimal air bubbles. The cap on the staging syringe is replaced by a connector used to fill the tubing. The plunger for the 3 mL syringe is installed and pushed all the way to the bottom removing all air. The two syringes are connected, and ink is transferred into the 3 mL syringe without introducing more bubbles. Next, a printing tip or nozzle is chosen for the application and is attached to the 3 mL syringe. The two nozzles used in this study are shown in Fig. 11. The syringe assembly is put together as shown in Fig. 10 and is ready to be mounted into the robocasting printer as shown in Fig. 12. The syringe is mounted onto the printer by two mounting plates and the plunger is attached to the piston by a threaded nut. The nozzle is friction held into a stage connected to an Aerotech assembly controlling motion in the x, y, and z planes. A removable substrate is secured in the oil bath.

For the HA scaffolds, 45 of the circular models were printed, as shown in Fig. 13, and dried in a fume hood. They were split into 3 groups of 15 scaffolds for sintering. For the HA/PMMA scaffolds, 75 of the square models were printed and dried in a fume hood. They were split into 5 groups of 15 scaffolds for each HA/PMMA ratio. Examples of the two scaffold types are shown in Fig. 14.

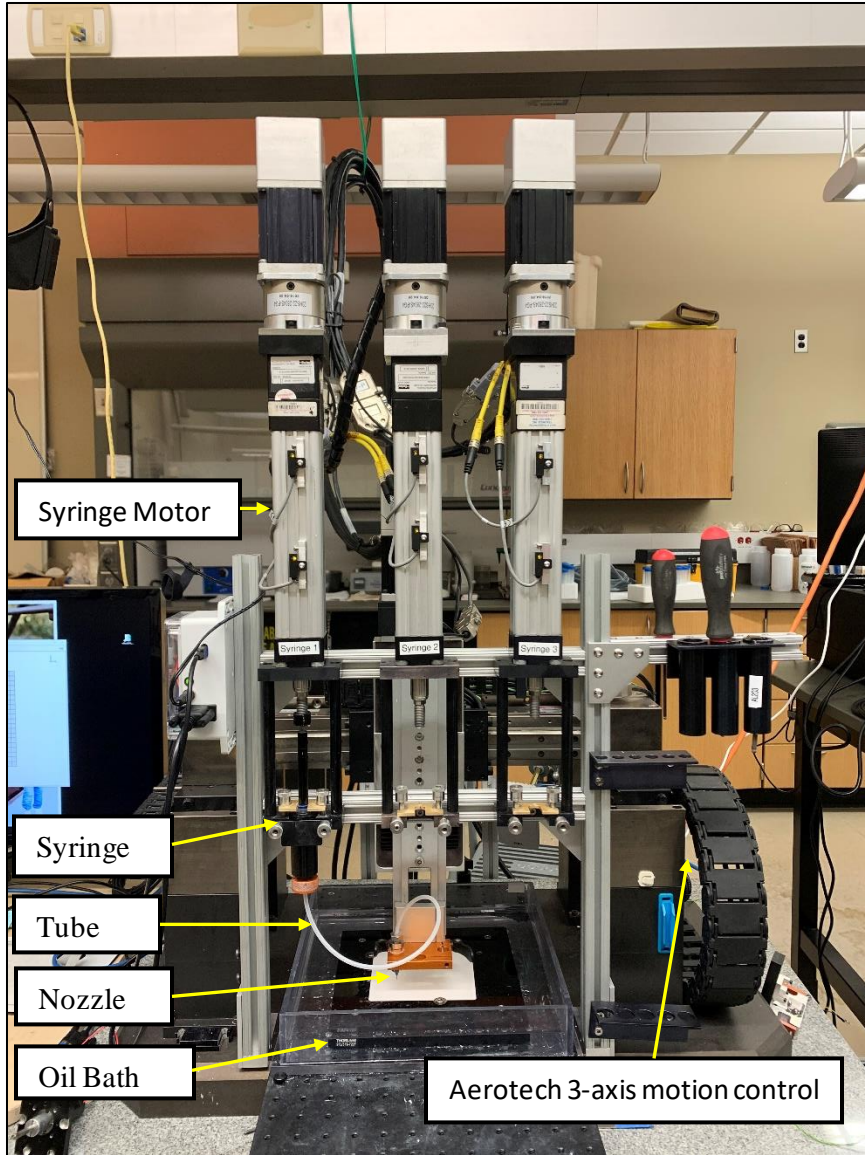


Figure 8: The robocasting printer in the Smay Lab.

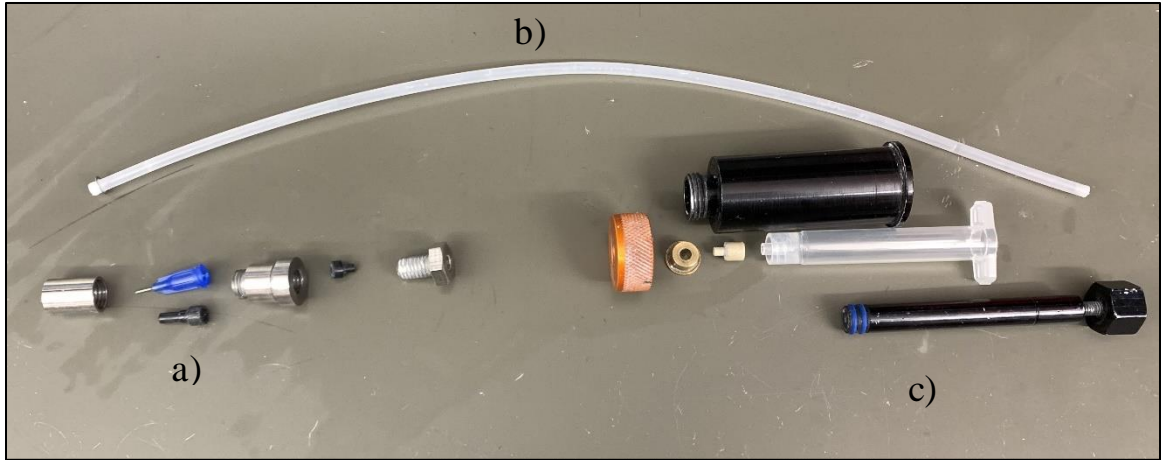


Figure 9: Constituent parts of the ink syringe assembly: a) the nozzle assembly, b) the tube and c) the ink syringe assembly.

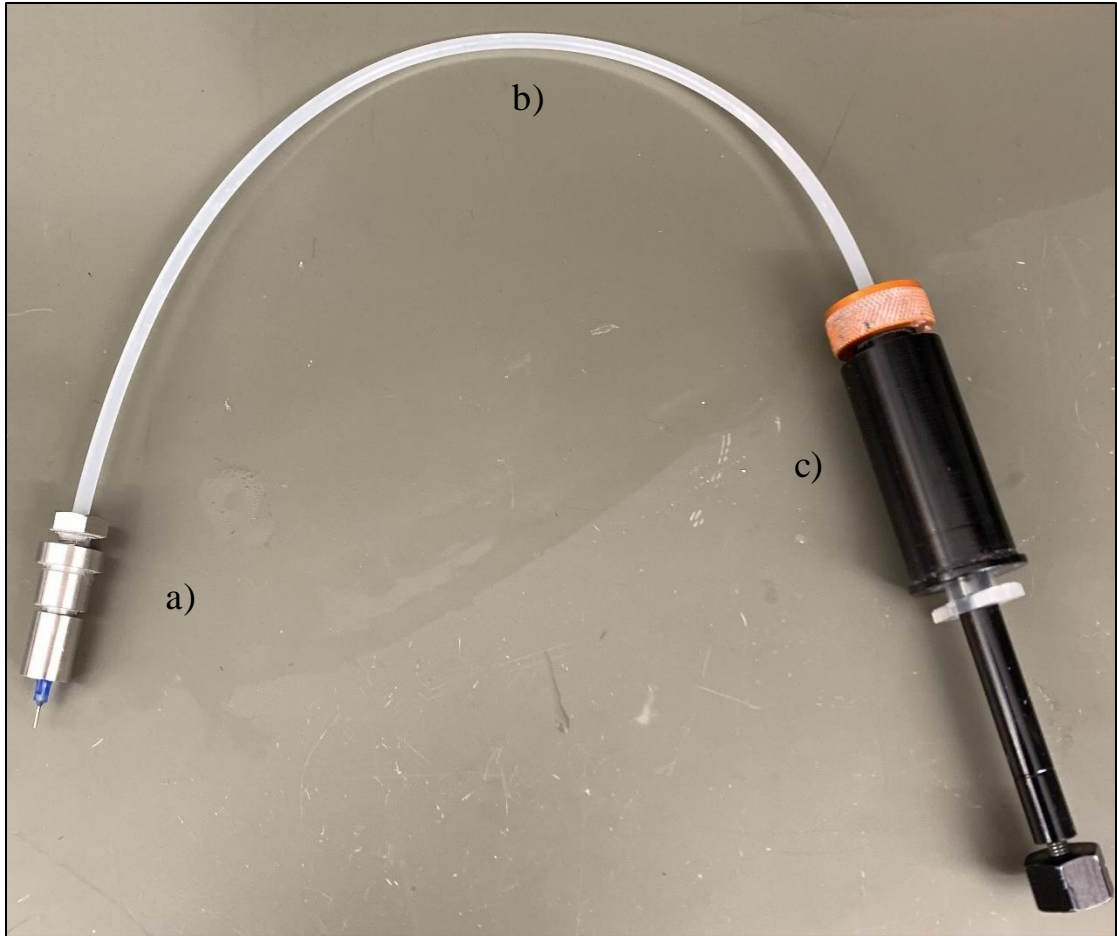


Figure 10: Ink syringe and nozzle fully assembled: a) the nozzle, b) the tube and c) the syringe.

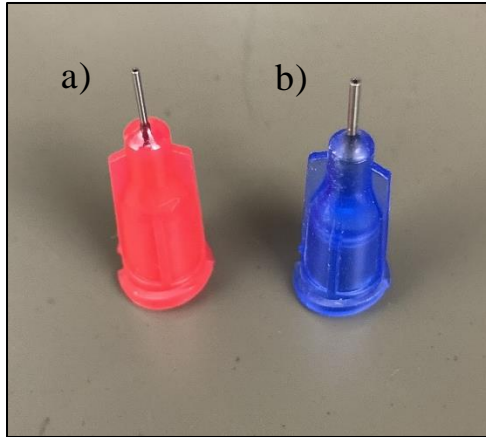


Figure 11: Robocasting nozzles: a) Red tip with a 250 μm diameter nozzle and b) Blue tip with a 410 μm diameter nozzle.

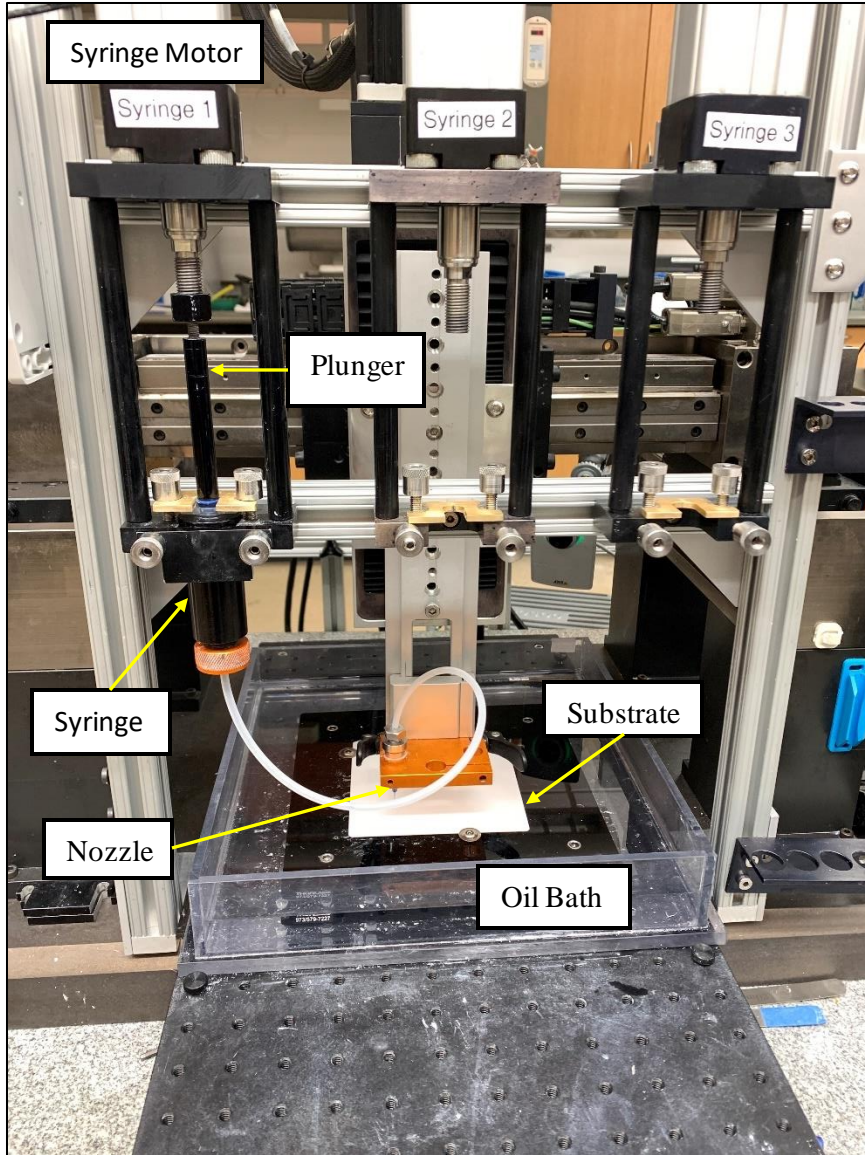


Figure 12: Ink Syringe and Nozzle mounted and secured in the robocast printer.

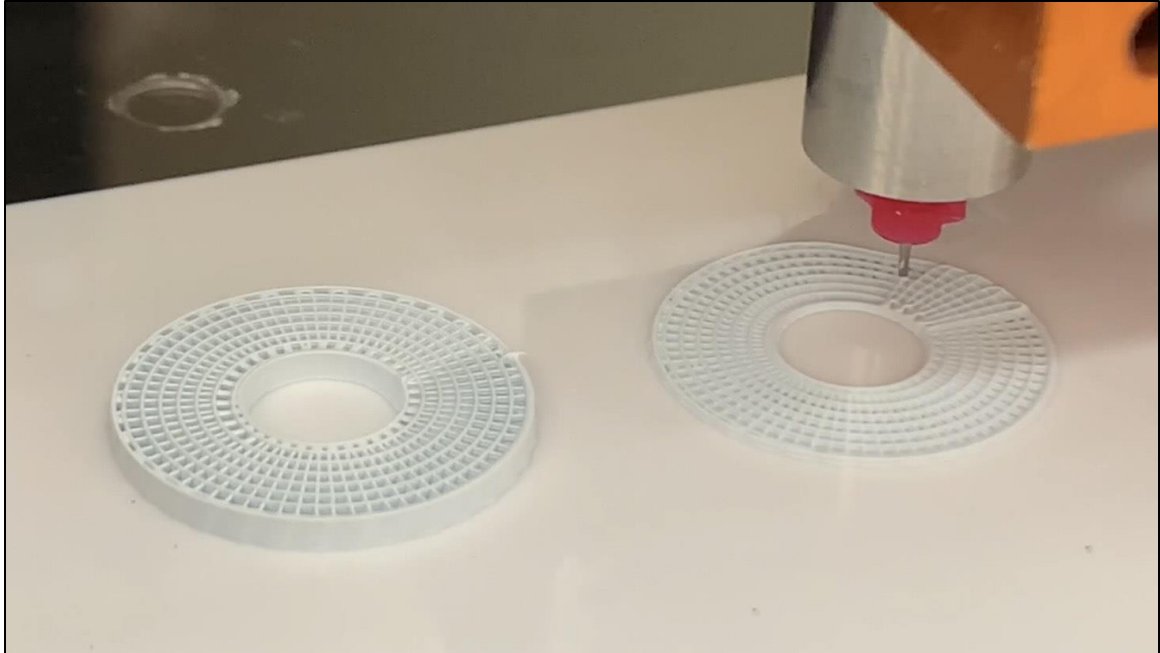


Figure 13: Robocasting in action (nozzle shown has a 250 μm tip diameter).

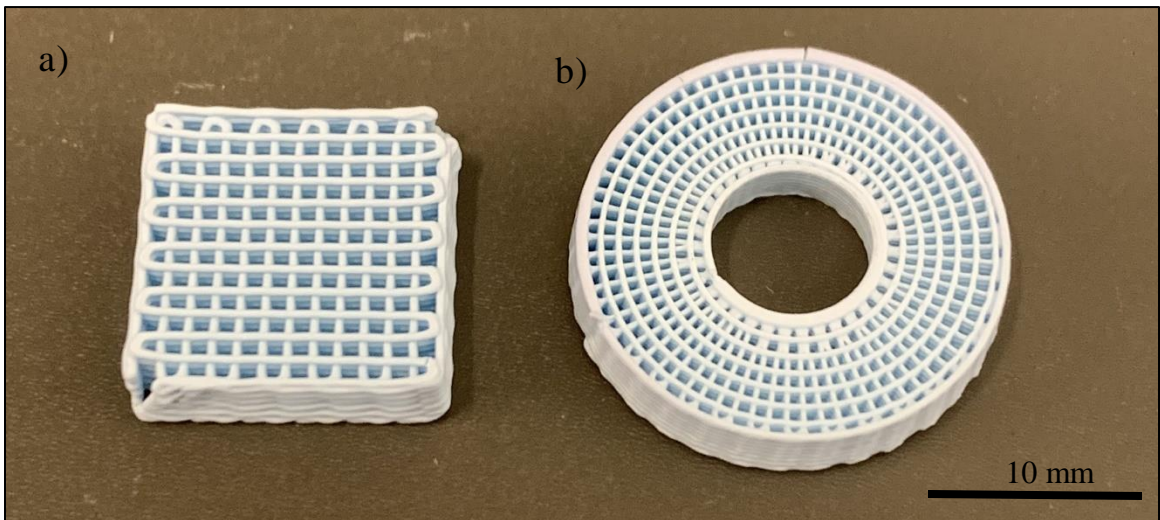


Figure 14: RoboCad models from Figure 6 fabricated with Robocasting: a) HA/PMMA Scaffold from a 410 μm tip and b) HA Scaffold from a 250 μm tip.

2.5 Solvent Leaching

Once the green state scaffolds containing PMMA powder have been given three days to adequately dry out, they are ready for a solvent leaching process to remove the PMMA particles from the ceramic structure. The solvent used is dichloromethane anhydrous (DCM), CH_2Cl_2 , manufactured by Sigma-Aldrich, Co. DCM is commercially available with <99.9% purity and contains 40-150 ppm amylene as a stabilizer. Scaffolds were placed in crucibles for the leaching process for two reasons. The crucible has a side wall taller than the height of the scaffolds, allowing the solvent to fill the crucible and submerge the scaffolds for optimal interaction between the DCM and PMMA. The leaching process dissolves the PMMA into solution and, as the solution evaporates, drapes a film of plastic onto all surfaces, effectively bonding the scaffolds to the crucible. The green state scaffolds are fragile and cannot be consistently removed without damage, so this step must take place in a vessel that can withstand sintering temperatures. The crucible and scaffolds, pictured in Fig. 15, are ready for sintering.

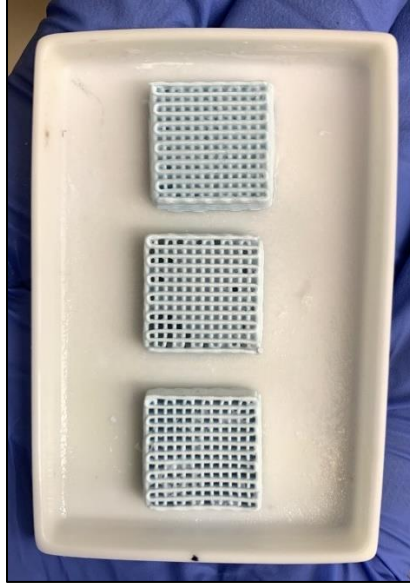


Figure 15: 85/15 HA/PMMA Scaffolds after the leaching process. Note the plastic film covering some of the scaffold voids.

2.6 Sintering

The green state scaffolds were ready for the sintering step after given three days to completely dry in air in a fume hood. HA is highly sintered at 1200°C and requires 4 hours at this temperature to complete the densification process. HA partially densifies between 1100°C (the calcination temperature) and 1200°C .

The HA scaffolds were divided into 3 groups of 15 and sintered at 1200°C , 1175°C , and 1150°C for 4 hours each to study porosity as a function of sintering temperature

The HA/PMMA scaffolds were printed as 5 groups of 15 and each were highly sintered at 1200°C for 4 hours. The 5 groups are characterized by HA/PMMA ratios of 95/5, 85/15, 75/25, 60/40, and 50/50 to allow a study porosity as function of pore former

inclusion. However, the ramp up to 1200°C needs to be modulated to allow a successful burnout of the PMMA. The solvent leaching removed most of the PMMA volume in the ceramic rods, but it is assumed a non-negligible amount of PMMA remains in the porous network. A sintering profile was created based on a TGA analysis of the Transoptic PMMA powder, shown in Fig. 16. This sintering profile features a slow temperature ramp up through the thermal degradation and mass loss zone and holds at 450°C for a low temperature burnout just beyond this zone. Later, the temperature is held again for a high temperature burnout at 900°C to completely remove any lingering degradation species.

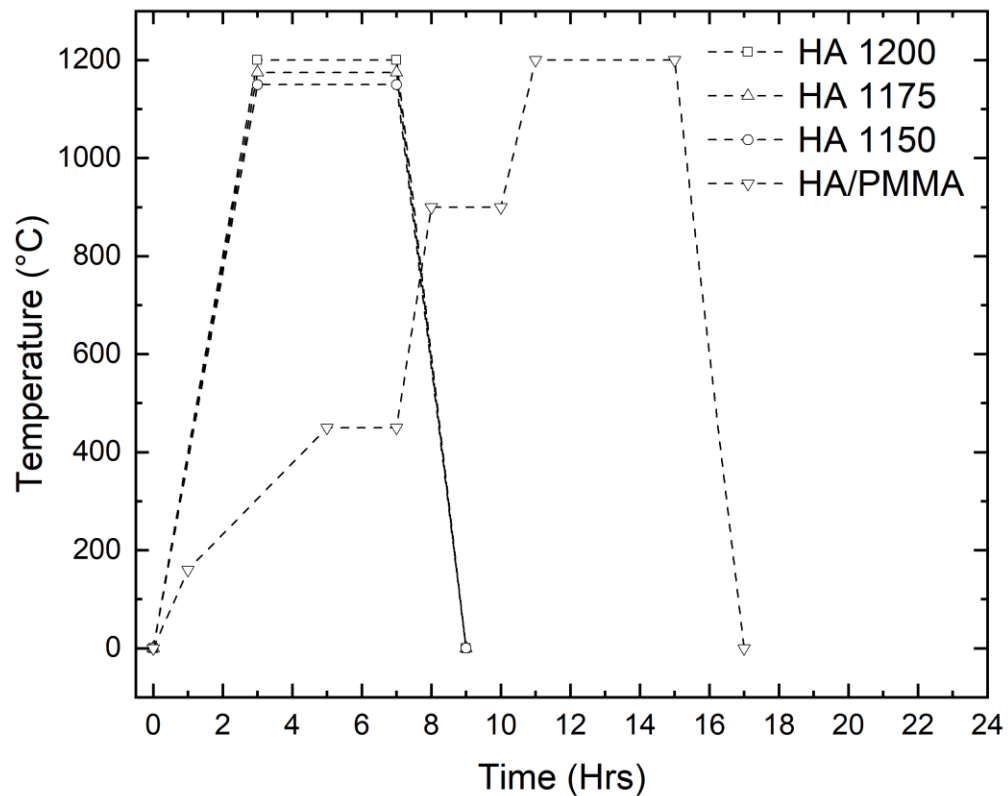


Figure 16: Sintering profiles for HA and HA/PMMA scaffolds.

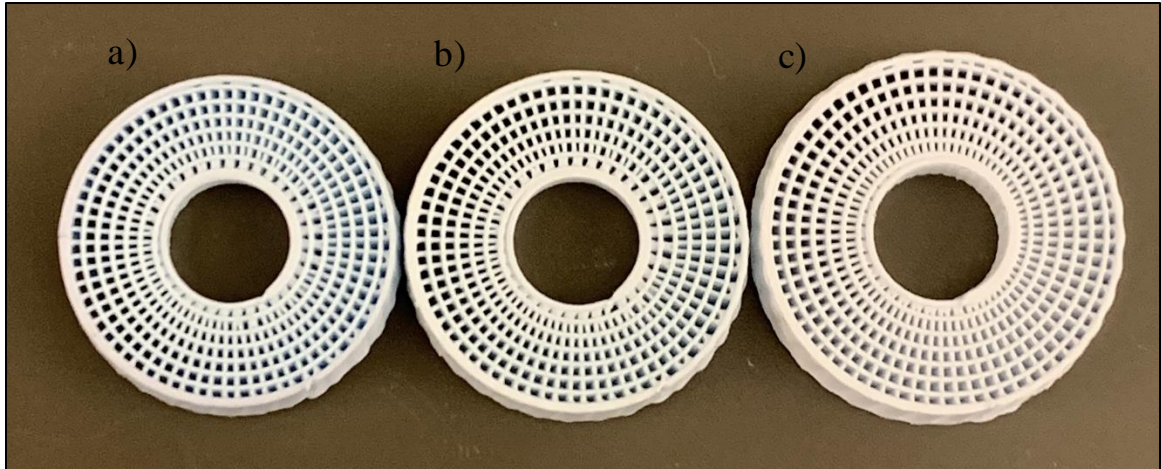


Figure 17: HA Scaffolds with same original dimensions showing varying amounts of densification due to sintering temperature: a) 1200°C, b) 1175°C and c) 1150°C.

2.7 Archimedes Method

Archimedes method is a simple way of determining density and volume for complex, porous geometries. These values can be used to determine total porosity, structural porosity, ceramic rod porosity, and open and closed porosity. First, a sample is weighed dry. Next, the sample is weighed while submerged in water. To get accurate values in this step, the sample needs to be degassed. In this study, the scaffolds were boiled for 20 minutes to properly displace any air in pore spaces with water. The submerged weight is measured using the Mettler Toledo Density kit. The volume of water the sample is submerged in is not on the scale, so the submerged weight is the weight of the sample dry subtracted by the upwards buoyancy force. The buoyancy force depends on the volume of water displaced by the scaffold, thus revealing the volume of the sample. Next, the sample is loosely dried off, leaving only water remaining in the ceramic and intermediate pore spaces. The weight of the sample at this point is the

saturated weight. The scaffold's true density was determined using the following equation for evaluating density using the Archimedes method [34]:

$$\rho_{true} = \frac{m_{dry}}{m_{dry} - m_{submerged}} * (\rho_{water} - \rho_{air}) + \rho_{air} \quad (7)$$

The density found in the above formula is specific to the scaffold and can be used with the bulk density of HA to determine closed porosity:

$$\Phi_{closed} = \left(1 - \frac{\rho_{sample}}{\rho_{bulk}}\right) * 100 \quad (8)$$

Finding the open porosity (Φ_{open}) requires more effort. First, the submerged mass ($m_{submerged}$) is subtracted by the dry mass (m_{dry}), leaving only the mass of the water inside the pore spaces (m_{water}). The water mass is multiplied by the density of water, leaving the volume of the occupied water in the pores (V_{water}). Next, we assign this volume as hydroxyapatite (V_{HA}) and multiple by the bulk density of HA (ρ_{bulk}) to give the mass of HA ($m_{extraHA}$) that could fill the pores. By filling the HA scaffold's pores with HA, we create fully dense HA rods that make up the scaffold ($m_{bulk scaffold}$). This mass is called the bulk scaffold mass and calculating the open porosity is as follows:

$$\Phi_{open} = \left(1 - \frac{m_{dry}}{m_{scaffoldbulk}}\right) * 100 \quad (9)$$



Figure 18: Mettler Toledo Density Kit for Archimedes analysis. Note the submerged scaffold for obtaining $m_{\text{submerged}}$.

The porosity of the ceramic rods themselves can be found by adding closed and open porosities:

$$\phi_{\text{ceramicrods}} = \phi_{\text{closed}} + \phi_{\text{open}} \quad (10)$$

The total porosity of the scaffolds can be measured by doing a geometrical volume analysis. This simply consists of measuring the sintered scaffold dimensions and

calculating a total volume. Combined with the mass of the dry sample, a theoretical total porosity can be calculated:

$$\rho_{scaffold} = \frac{m_{dry}}{V_{Total}} \quad (11)$$

$$\Phi_{Total} = \left(1 - \frac{\rho_{scaffold}}{\rho_{bulk}}\right) * 100 \quad (12)$$

Additionally, the structural porosity can be derived from the data as well. It is calculated by a simple porosity formula between $m_{scaffoldbulk}$ and m_{bulk} :

$$\Phi_{macro} = \left(1 - \frac{m_{bulkscaffold}}{m_{bulk}}\right) * 100 \quad (13)$$

To create a statistically robust model ten scaffolds of each kind, over 80 total, were measured using Archimedes method.

2.8 Backscattering Electron Microscopy (BSE)

A representative sample of each scaffold type was selected to examine with backscattering electron microscopy (BSE). The scaffolds were degassed in a vacuum chamber and embedded with an EpoFix epoxy. Next the scaffolds were cut in half to expose the cross-section view of the ceramic rods comprising the scaffolds. BSE requires a mirror finish, so the cross-section faces were polished with increasingly fine sandpaper grit and finished with a 1 μm diamond colloid gel. The mirror finishes were then

sputtered with iridium to give the electrons during BSE a conductive surface to dissipate over. Each scaffold was analyzed with BSE to evaluate each mode of porosity.

CHAPTER III

RESULTS

3.1 Helium Pycnometry

The standard density of hydroxyapatite is 3.16 g/cm^3 . [35] However, to get accurate data for the specific HA powder used in this study, a gas pycnometry test using helium was performed. Average density was found to be 3.0837 g/cm^3 with a standard deviation of 0.0083 g/cm^3 .

3.2 Thermal Analysis for PMMA

After the leaching process, it is safe to assume some significant percentage of original PMMA content remains in the green state scaffolds which needs to be burned out during the sintering stage. Identifying the temperatures that coincide with phase change and mass loss allow a customized sintering cycle to be fitted to scaffolds containing the PMMA powder in which the PMMA can be removed from the scaffold in a nondestructive manner. Thermogravimetric analysis (TGA) heats a material on a scale and records when mass loss occurs. The TGA curve for the PMMA powder shows that mass loss begins around 200°C and becomes significant at roughly 225°C , as shown in Fig 19. Differential scanning calorimetry (DSC) measures the temperature of a sample as

heat rises in a chamber and records any periods of latent heating, which is interpreted as a phase change. The DSC curve for PMMA is somewhat difficult to understand but appears to show a phase change at 115°C as shown in Fig 20. The TGA curve was only used in determining the sintering cycle.

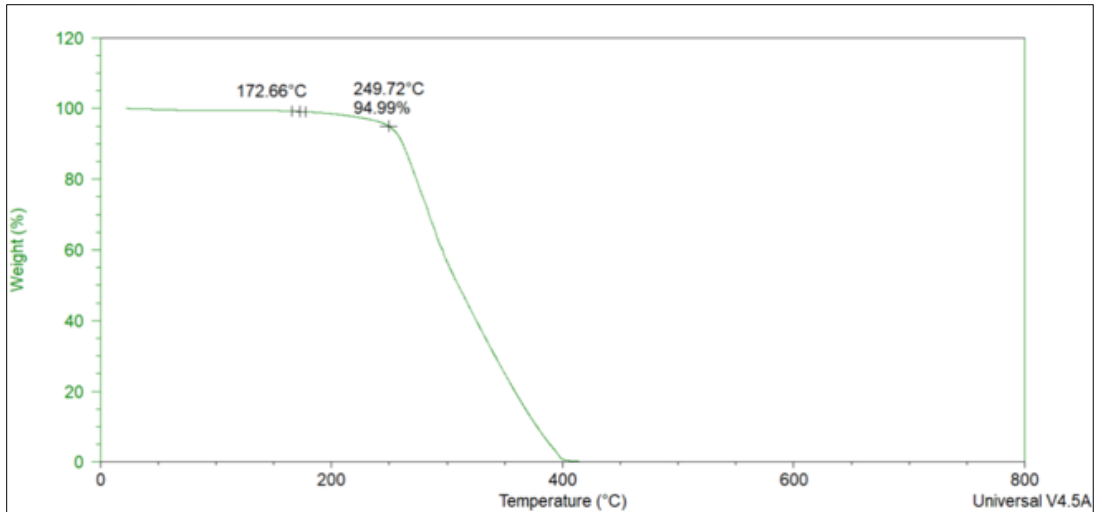


Figure 19: TGA curve for Transoptic PMMA powder.

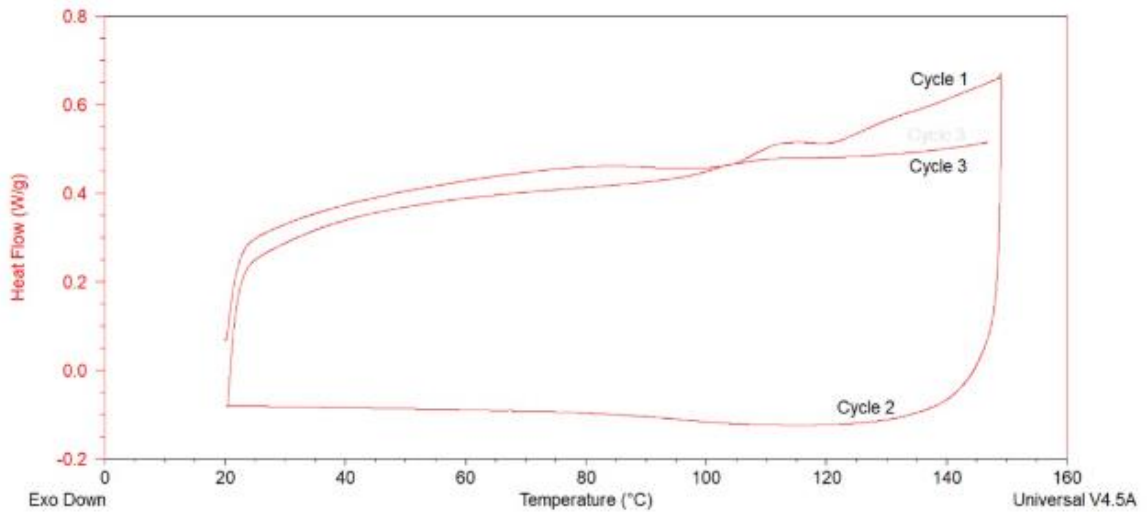


Figure 20: DSC curve for Transoptic PMMA powder.

3.3 Archimedes Density Testing

Archimedes testing for each scaffold type was performed 10 times to mitigate the effects of any defects caused by the printing, leaching, sintering, and boiling processes.

The data that is an average for 10 scaffolds includes an error bar in the graphs representing one standard deviation. The relevant data used in the graphs is shown in Table 3 below. With Archimedes method, total porosity, structural porosity, and ceramic rod open v. closed porosity have been calculated. Identifying the ratio of ceramic porosity and intermediate porosity within the ceramic rods has proven quite difficult and was not calculated.

Table 3: Relevant data from the Archimedes method.

Sample	m_{dry} (g)	$m_{submerged}$ (g)	$m_{saturated}$ (g)	ρ_{true} (g/cm ³)	Φ_{Total} (%)	$\Phi_{structural}$ (%)	Φ_{open} (%)	Φ_{closed} (%)	$\Phi_{ceramicrod}$ (%)
1200°C	0.583	0.397	0.656	3.13	67.54	50.6	27.9	1.06	29.0
1175°C	0.524	0.356	0.618	3.12	72.68	57.6	35.7	1.31	37.0
1150°C	0.531	0.36	0.641	3.1	73.01	59.7	39.0	1.93	40.9
100/0	0.446	0.305	0.482	3.16	66.9	58.7	19.9	0.107	20.0
95/5	0.404	0.274	0.458	3.10	71.9	60.3	29.0	1.97	30.9
85/15	0.377	0.252	0.426	3.01	73.5	62.8	28.7	4.87	33.6
75/25	0.329	0.217	0.375	2.95	76.2	65.8	30.3	6.54	36.8
60/40	0.255	0.160	0.299	2.69	80.6	70.0	34.4	15.0	49.4
50/50	0.285	0.184	0.366	2.81	77.3	57.3	46.4	10.9	57.3

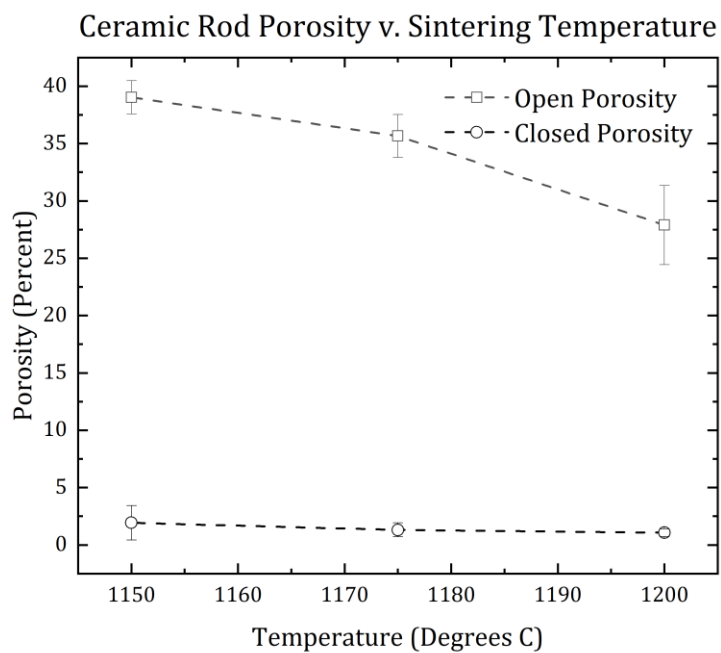


Figure 21: Ceramic rod porosity of HA scaffolds determined by Archimedes testing.

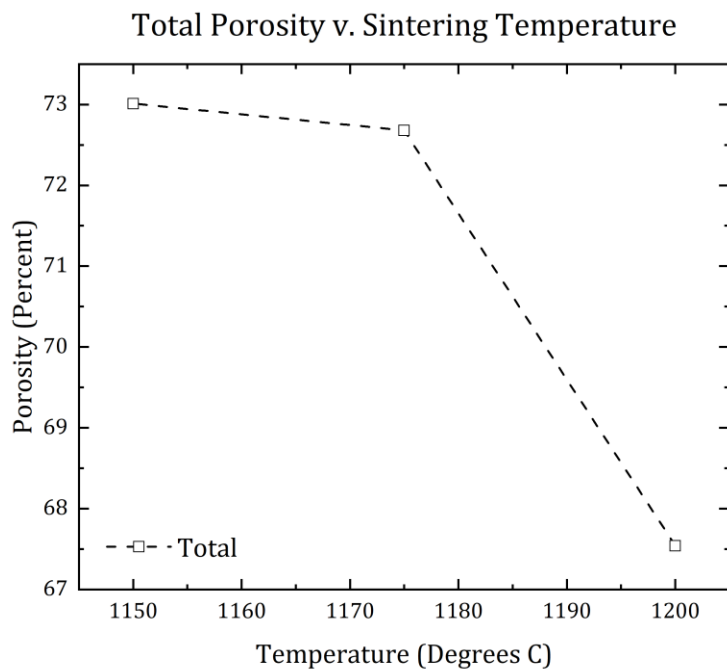


Figure 22: Total porosity of HA scaffolds determined by volumetric analysis.

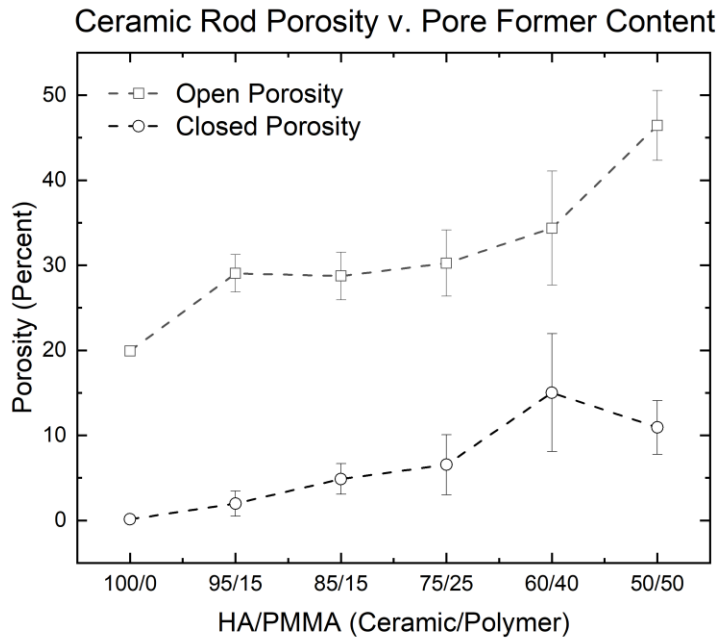


Figure 23: Ceramic rod porosity of HA/PMMA scaffolds determined by the Archimedes method.

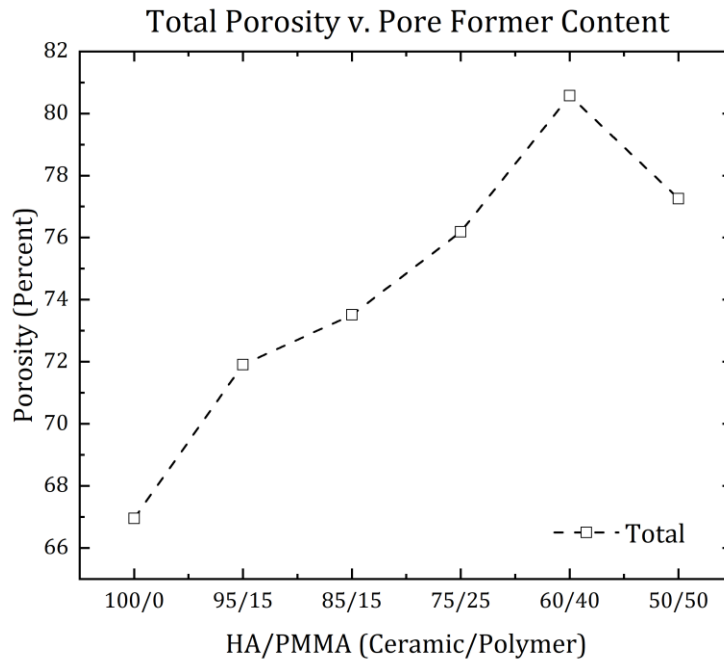


Figure 24: Total Porosity of HA/PMMA scaffolds determined by volumetric analysis.

The graphs showing the Archimedes method data show clear porosity dependence on both sintering temperature and fugitive pore former content.

3.4 Mercury Intrusion Porosimetry

Mercury Intrusion Porosimetry (MIP) is used to determine bulk density, skeletal density, porosity, and show the pore size distribution of a sample. Bulk density is a low-pressure measurement at 0.20 psia while skeletal density is a high-pressure measurement at approximately 60,980 psia. The porosity and densities are shown in Table 4 and the pore size distributions are shown in Figures 25 and 26. The porosities are plotted in Figures 27 and 29. The densities are plotted in Figures 28 and 30.

Table 4: Data acquired from MIP.

Sample	Bulk Density (g/mL)	Skeletal Density (g/mL)	Porosity (%)
1200	1.8694	3.1091	39.8743
1175	1.6387	3.1426	47.8543
1150	1.4852	3.1539	52.9088
95/5	2.1595	3.1871	32.2429
85/15	1.5023	3.1269	51.9565
75/25	1.3506	3.0202	55.2803
60/40	1.1484	2.6287	56.3122
50/50	1.0502	2.7133	61.2948

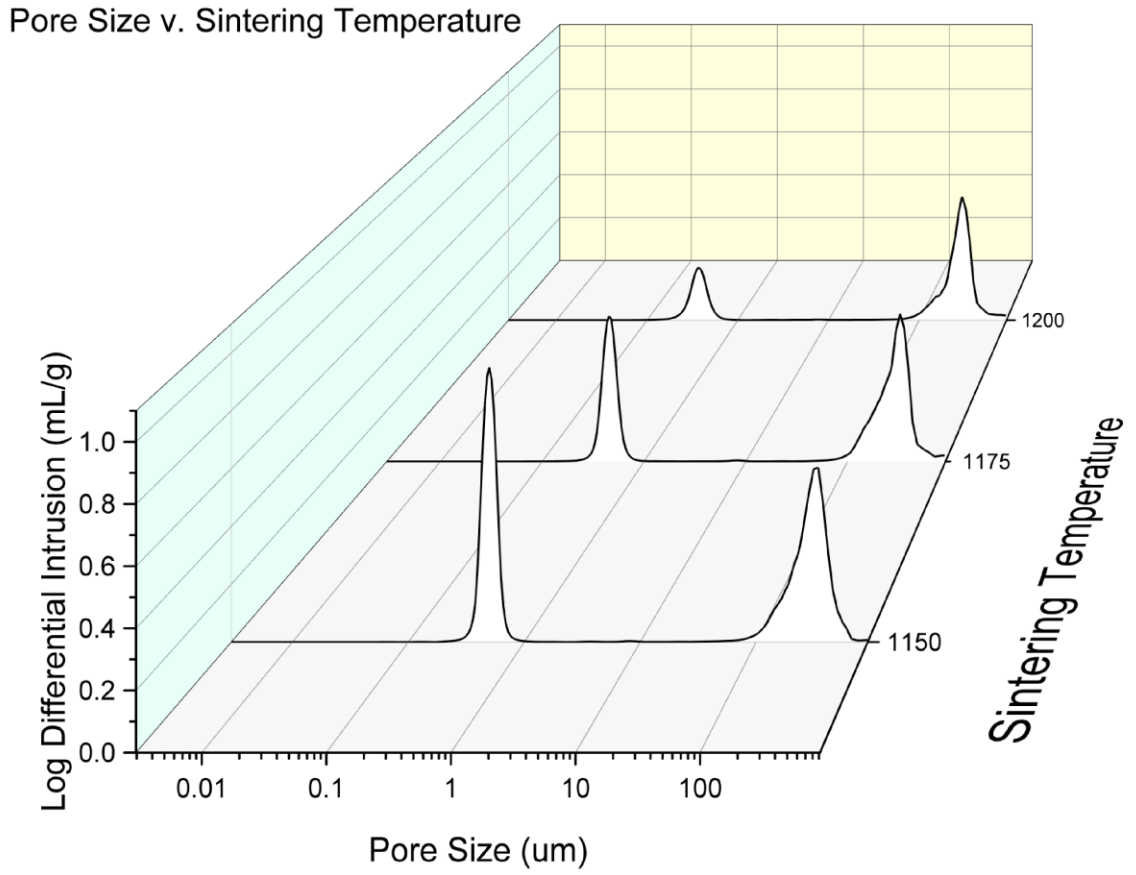


Figure 25: Bimodal pore size distribution for the HA scaffolds determined by MIP.

Pore Size v. Scaffold Composition

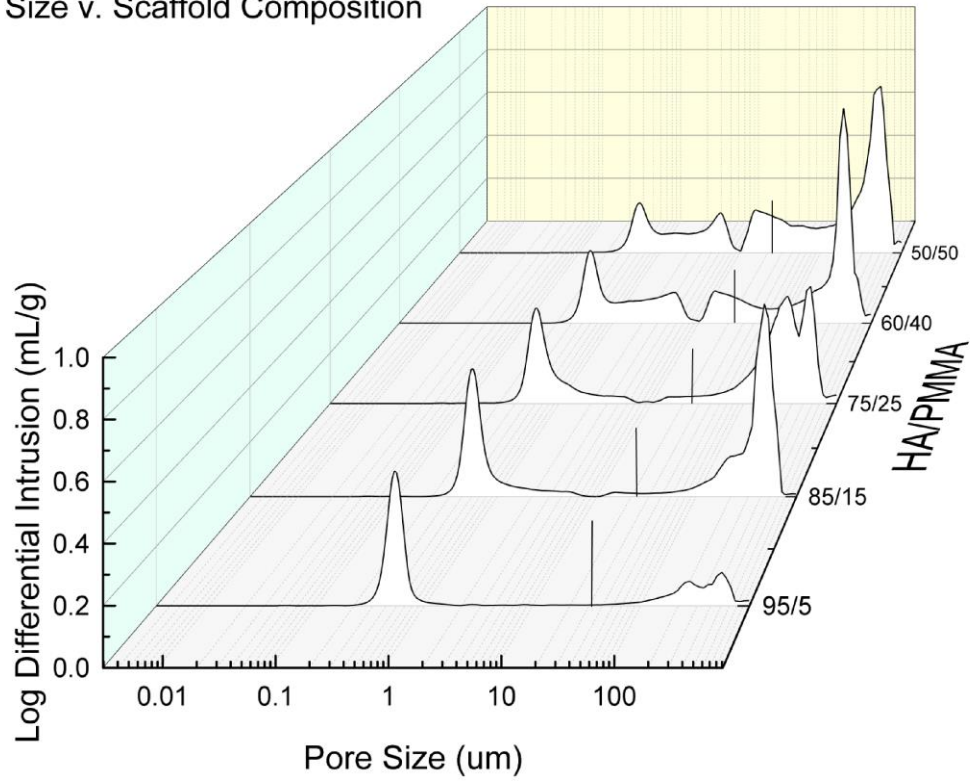


Figure 26: Distribution of pore sizes as pore former content is increased during MIP. Note the vertical lines marking the average intermediate pore diameter from BSE.

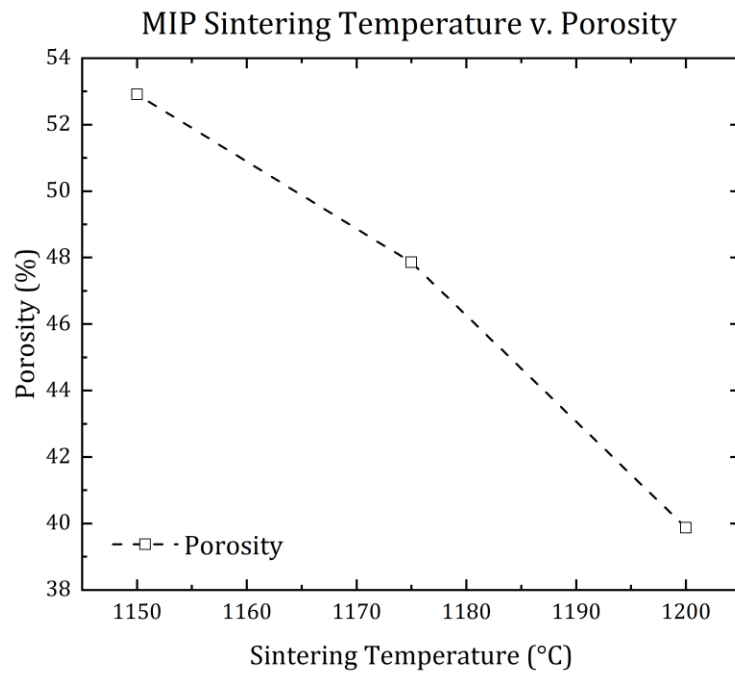


Figure 27: MIP Porosity variation due sintering temperature.

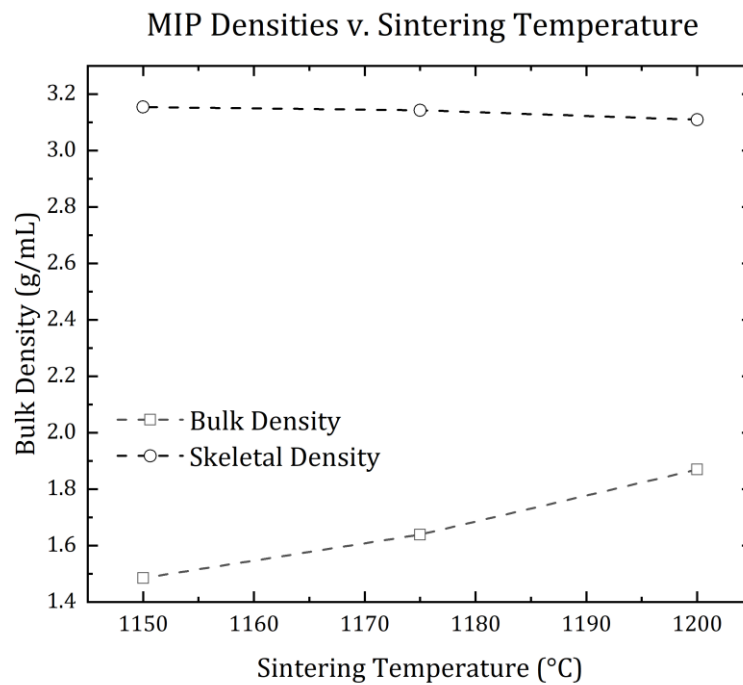


Figure 28: MIP densities variation due to sintering temperature.

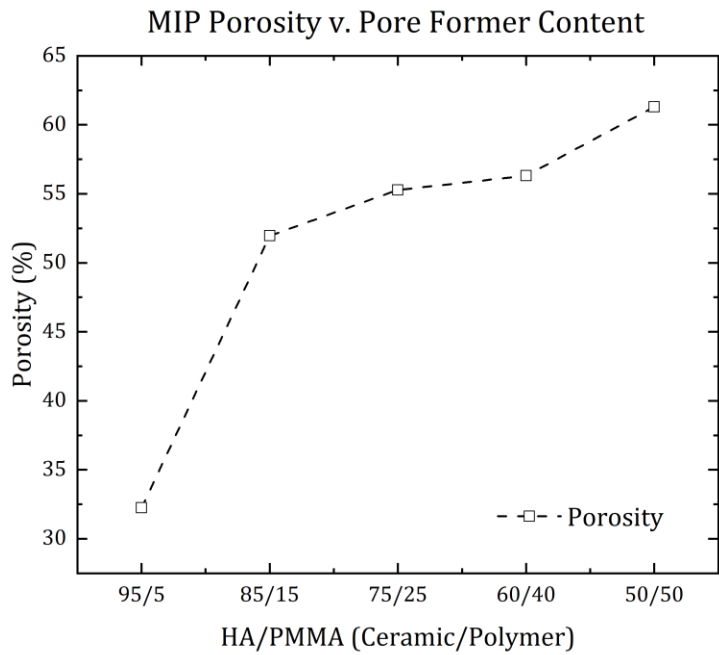


Figure 29: MIP Porosity variation due to pore former content.

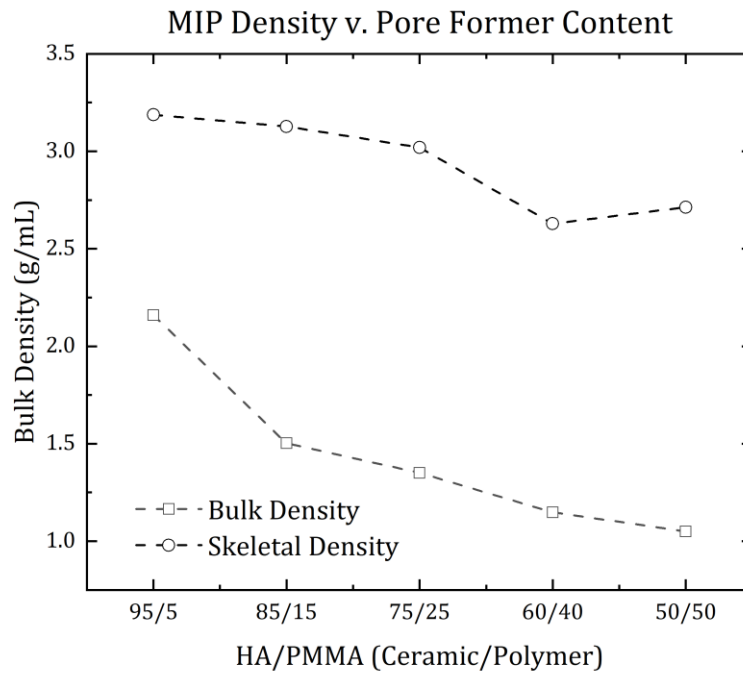


Figure 30: MIP densities variation due to pore former content.

3.5 Scanning Electron Microscopy (SEM) Images

Scanning Electron Microscopy (SEM) was used to demonstrate the spherical nature of the Transoptic PMMA powder used as fugitive pore former in this study. Also, the powder was sieved to include only particles below 65 μm , which is backed up by the SEM image.

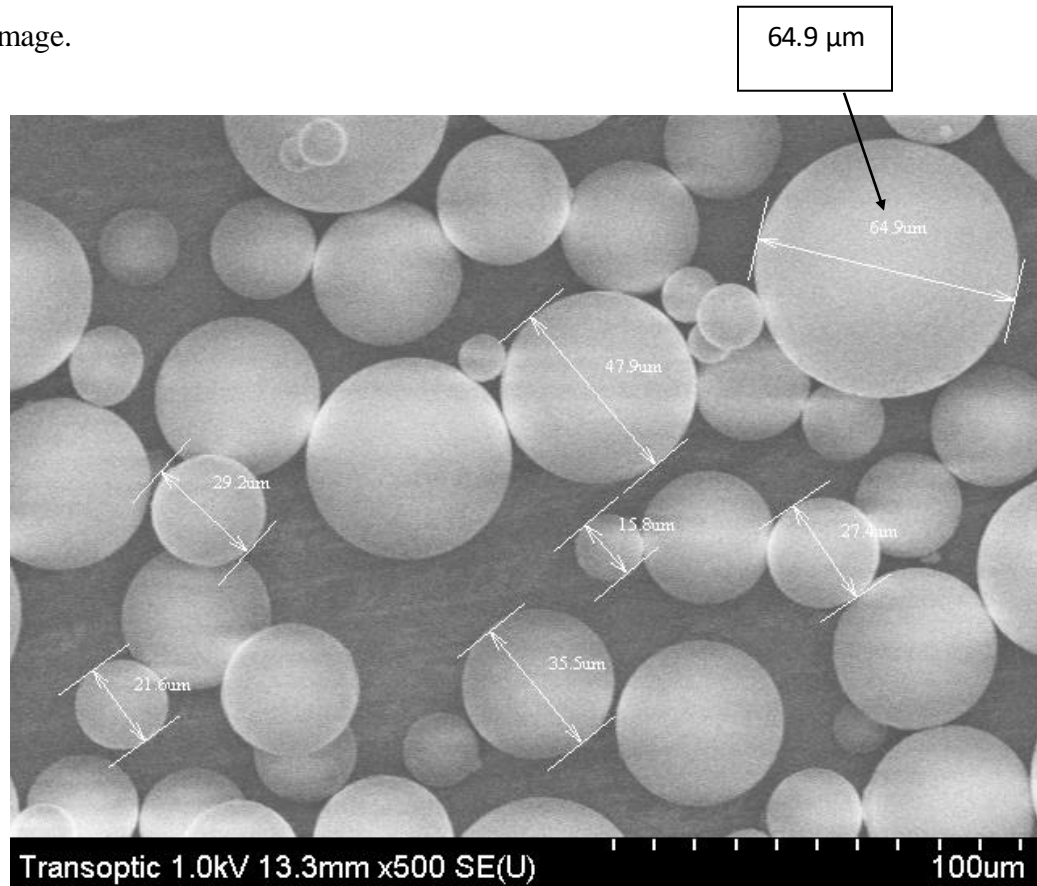


Figure 31: SEM image of Transoptic PMMA.

3.6 Backscattered Electron Imaging (BSE)

BSE images performed on the HA scaffolds are displayed in Table 5 and images for the HA/PMMA scaffolds are displayed in Table 6.

Table 5: BSE results for HA scaffolds.

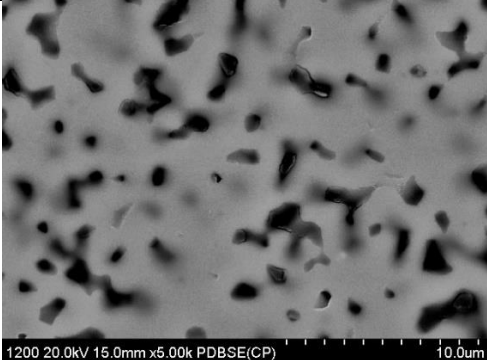
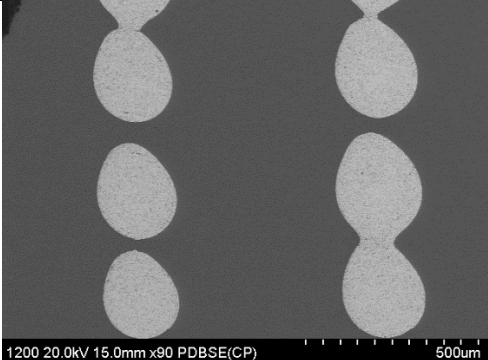
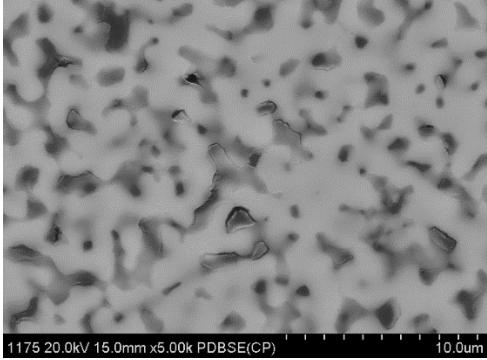
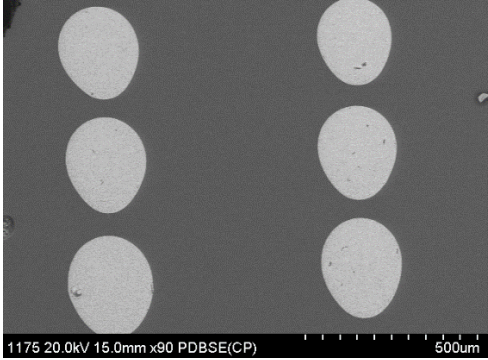
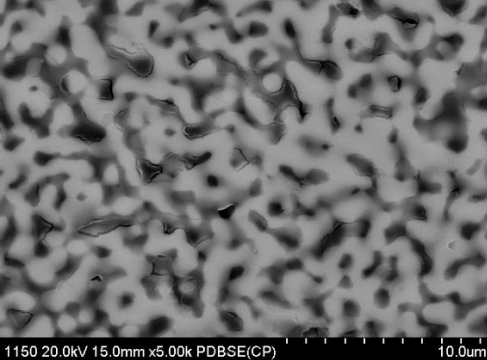
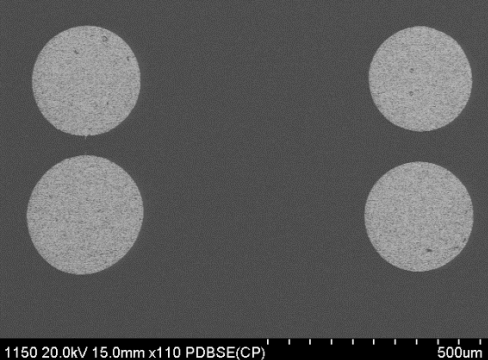
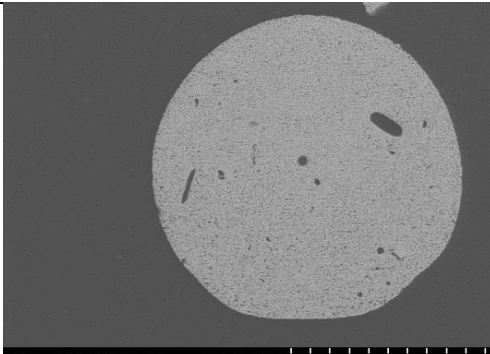
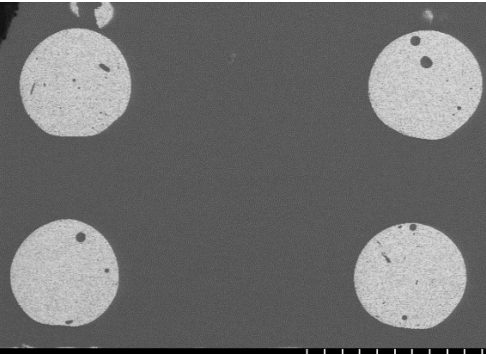
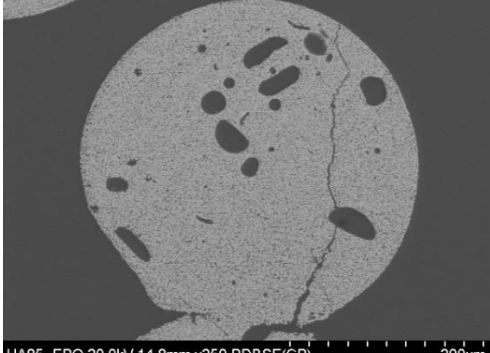
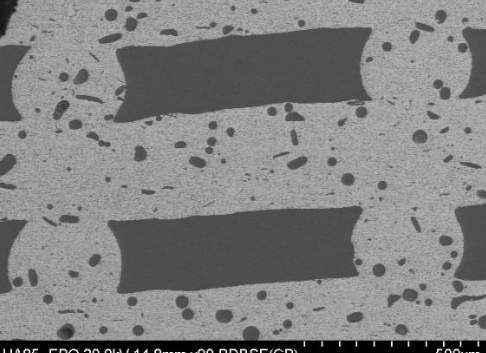
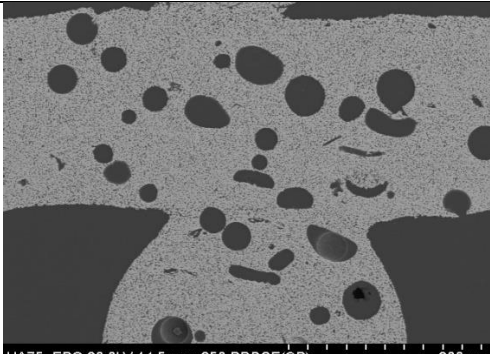
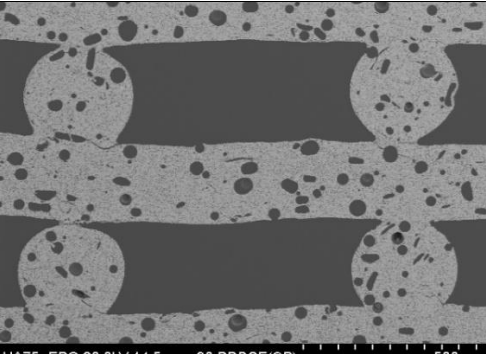
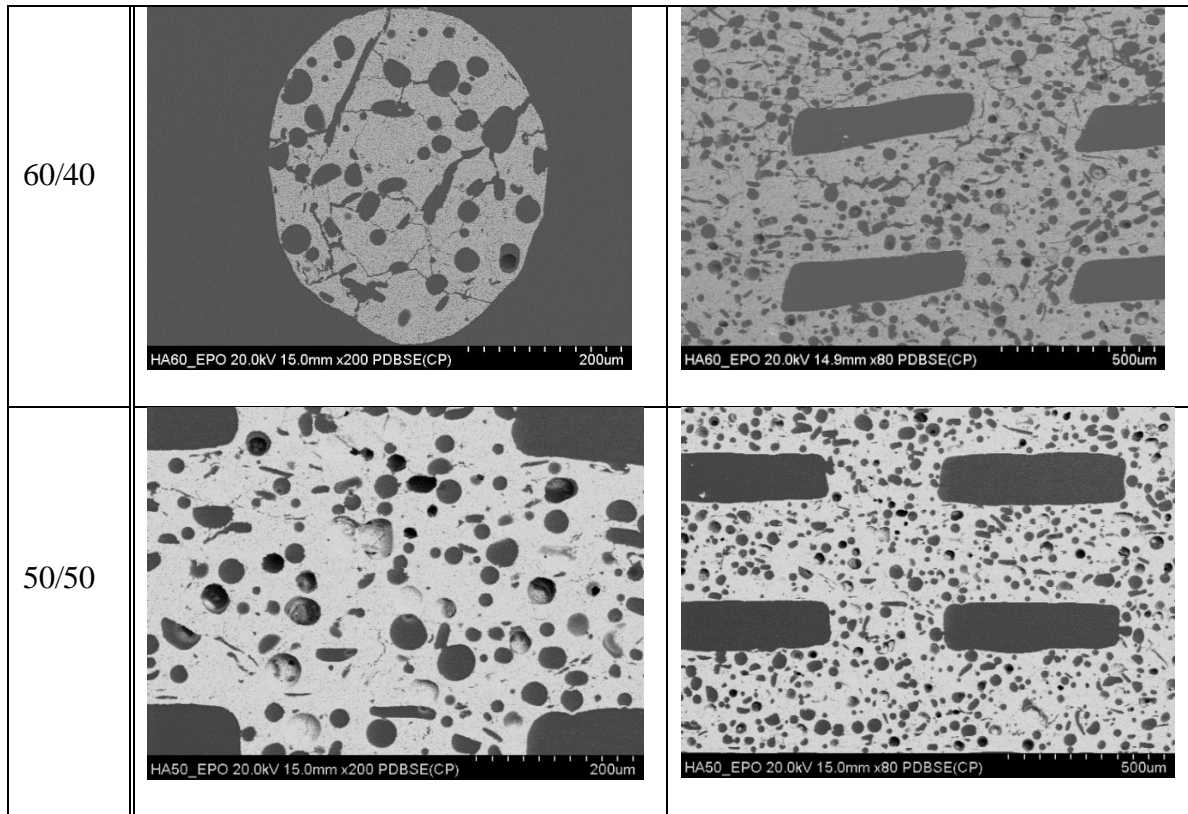
Sample	Ceramic Porosity	Structural Porosity
1200		
1175		
1150		

Table 6: BSE results for HA/PMMA scaffolds.

Sample	Intermediate Porosity	Structural Porosity
95/5	 <p>HA95_EPO 20.0kV 14.8mm x250 PDBSE(CP) 200µm</p>	 <p>HA95_EPO 20.0kV 14.8mm x90 PDBSE(CP) 500µm</p>
85/15	 <p>HA85_EPO 20.0kV 14.8mm x250 PDBSE(CP) 200µm</p>	 <p>HA85_EPO 20.0kV 14.8mm x90 PDBSE(CP) 500µm</p>
75/25	 <p>HA75_EPO 20.0kV 14.5mm x250 PDBSE(CP) 200µm</p>	 <p>HA75_EPO 20.0kV 14.5mm x90 PDBSE(CP) 500µm</p>



3.7 ImageJ Pore Size Analysis

The backscattered electron microscopy (BSE) images were analyzed using an image processing software called ImageJ. This software allows the pores in an image to be analyzed and calculates an average pore diameter. The results for each scaffold are shown in Table 7 below. The average pore diameters for the HA/PMMA scaffolds were overlaid onto the MIP pore size distribution charts to show the intermediate pore sizes where the MIP artifact occurs.

Table 7: Pore size Analysis Data performed by ImageJ.

Sample	Count	Total Area (μm^2)	Average Size (μm^2)	Area (%)	Average Diameter (μm)
1200	1679	2919.7	1.74	25.93	1.488
1175	2099	3436.895	1.64	30.59	1.444
1150	2989	5014.943	1.68	36.13	1.462
95/5	31	23527.105	758.9	0.525	31.086
85/15	154	67722.686	439.8	4.88	23.663
75/25	198	112824.817	569.8	8.15	26.936
60/40	818	382553.366	467.7	21.86	24.402
50/50	918	386855.454	421.4	22.17	23.164

3.8 Failed Experiments

There were two areas of this study that were not able to be accomplished as planned. The first area was the method for removing the PMMA pore former from the green state scaffolds. The original plan was to do incorporate a comprehensive burnout into the sintering program. The PMMA would degrade and volatilize and exit the scaffold at high temperatures. However, this was never accomplished successfully due to green state scaffold destruction during this process. The second area was with the data processing from the Archimedes method. Ideally, exact percentages of the total porosity

would have been calculated and assigned to ceramic porosity, intermediate porosity, and structural porosity. The most specific the total porosity was able to be evaluated was into structural porosity and ceramic rod porosity. Distinguishing ceramic porosity and intermediate porosity from the ceramic rod porosity proved quite difficult.

CHAPTER IV

DISCUSSION

4.1 Archimedes Method

The Archimedes method is a powerful technique for analyzing scaffolds with multiple modes of porosity. There might be a way to find porosity of all three modes using Archimedes, but in this study, it was used to find total porosity, structural porosity, ceramic rod porosity, and open and closed porosity. The data from Archimedes shows all modes of porosity are decreased with higher sintering temperatures compared to lower temperatures. Similarly, it established a clear upward trend in porosity as pore former volume fraction was increased.

4.2 MIP

The pore size v. sintering temperature chart, Fig. 25, for the HA scaffolds shows a clear bimodal pore size distribution at approximately 0.5 μm and 350 μm . This is a clear representation of the ceramic porosity and the structural porosity. From lower to higher sintering temperatures, the structural porosity is unaffected while the ceramic porosity significantly decreases. This backs up the data found with the Archimedes method. However, the pore size v. pore former content, Fig. 26, essentially shows the same

bimodal distribution for the 95/5 scaffold, but with the edges not being as well defined. As the pore former content increases, the sharp bimodal distribution is lost and there are pores ranging in size between the ceramic and structural pores. This is the intermediate porosity. Unfortunately, there is an artifact in the MIP data where the system switches from low pressure to high pressure and some potentially important data for the intermediate pores was not able to be measured as a result. What can be said for certain is that the sharp bimodal pore size distribution from the HA only scaffolds is decreased due to the presence of intermediate pores and elevated pore connectivity.

The intermediate pore influence on the pore size v pore former content chart, Fig.26, is not significant until the 60/40 ratio. From this data, it can be surmised that the critical volume fraction of fugitive pore former required to form a percolating network occurs somewhere between 0.25 and 0.40.

4.3 BSE

BSE for the HA scaffolds confirms the MIP data. Ceramic porosity is dependent on sintering temperature and can be clearly seen in the BSE ceramic pores column in Table 5. BSE also shows how the structural porosity is largely unaffected by changes in sintering temperature.

BSE for the HA/PMMA scaffolds clearly shows the influence of intermediate pores on total porosity. Also, these images show many isolated intermediate pores (identified by a different contrast compared to the pores filled with epoxy), which corroborates the high closed porosity values measured with Archimedes method.

4.4 Ink Formulation

While degassing the scaffolds via boiling during the Archimedes density testing, the 60/40 scaffolds experienced a significant amount of disintegration. This was odd, since none of the 95/5, 85/15, or 75/25 scaffolds experienced anything similar. The BSE images of the 60/40 scaffolds show a dramatic increase in the number of cracks through the scaffold. Meaning, the compressive shear stress of the air-drying process was overpowering the flocculant's interparticle strength and compromised the structure with cracks. After a discussion in the lab, it was assumed that not enough PEI had been added. At lower pore former volume fractions, the PEI was sufficiently flocculating the ceramic particles, but at higher pore former fractions it is assumed the pore former was interfering with the flocculation strength between the ceramic particles. The 60/40 scaffolds were prepared with 6 drops of PEI. For the 50/50 scaffolds, the ink was prepared with 11 drops of PEI. The 50/50 scaffolds still had some disintegration during boiling, but significantly less than the 60/40 scaffolds. Even at a higher pore former volume fraction, the 50/50 was sufficiently flocculated to withstand the compressive shear stress from the drying process.

4.5 Future Work

An important finding in this study was establishing a zone in which a critical volume fraction of pore former creates a percolating network. Unfortunately, the zone is from 0.25 to 0.4 volume fraction, which is quite large. An important finding in a future study would be identifying the threshold volume fraction of pore former required to create the percolating network.

Another important finding in this study was the importance of PEI as pore former volume fraction is increased. By elevating PEI levels, one can intuit scaffolds with much higher pore former amounts could be attempted than those in this study.

Lastly, establishing a burnout method for the PMMA pore former would be ideal. Dichloromethane anhydrous is a carcinogenic chemical and, even though most likely none of it survives the sintering process, would potentially hinder scaffolds fabricated this in the eyes of the U.S. Food and Drug Administration (FDA). This could be avoided if the pore former is burned out of the scaffold during the sintering process.

CHAPTER V

CONCLUSION

Robocasting biocompatible synthetic bone scaffolds has a promising future in the field of tissue engineering. Due to the highly porous (75-95%) nature of the trabecular tissue where the healing in bone takes place, knowledge of how to fabricate and characterize porous synthetic scaffolds is essential. In this study, robocasting scaffolds with control over three modes of porosity is explored. Ceramic porosity was proven to decrease with high sintering temperature and increase at lower sintering temperature. Intermediate porosity is dependent on the volume fraction of Transoptic PMMA pore former included in the ink formulation, with the creation of a percolating network between 0.25 and 0.4 volume fraction. Structural porosity is controlled by CAD and is the largest contributor to total porosity.

This study established a clear method for robocasting scaffolds of known porosity, showed a range of porosity through sintering, showed a range of porosity through fugitive polymer spheres, and showed where the threshold volume fraction of fugitive polymer spheres occurs for achieving a percolating network.

REFERENCES

1. Bandyopadhyay, A., S. Bose, and S. Das, *3D printing of biomaterials*. MRS Bulletin, 2015. **40**(2): p. 108-115.
2. Tariverdian, T., et al., *10 - Scaffold for bone tissue engineering*, in *Handbook of Tissue Engineering Scaffolds: Volume One*, M. Mozafari, F. Sefat, and A. Atala, Editors. 2019, Woodhead Publishing. p. 189-209.
3. Wei, J., et al., *3D-printed hydroxyapatite microspheres reinforced PLGA scaffolds for bone regeneration*. Biomaterials Advances, 2022. **133**: p. 112618.
4. Roleček, J., et al., *Bioceramic scaffolds fabrication: Indirect 3D printing combined with ice-templating vs. robocasting*. Journal of the European Ceramic Society, 2019. **39**(4): p. 1595-1602.
5. Navarrete-Segado, P., et al., *Masked stereolithography of hydroxyapatite bioceramic scaffolds: From powder tailoring to evaluation of 3D printed parts properties*. Open Ceramics, 2022. **9**: p. 100235.
6. Indra, A., et al., *A novel fabrication procedure for producing high strength hydroxyapatite ceramic scaffolds with high porosity*. Ceramics International, 2021. **47**(19): p. 26991-27001.
7. Hassanajili, S., et al., *Preparation and characterization of PLA/PCL/HA composite scaffolds using indirect 3D printing for bone tissue engineering*. Materials Science and Engineering: C, 2019. **104**: p. 109960.
8. Wu, A.-M., et al., *Global, regional, and national burden of bone fractures in 204 countries and territories, 1990–2019: a systematic analysis from the Global Burden of Disease Study 2019*. The Lancet Healthy Longevity, 2021. **2**(9): p. e580-e592.
9. Magee, M.J. and K.M.V. Narayan, *Global confluence of infectious and non-communicable diseases — The case of type 2 diabetes*. Preventive Medicine, 2013. **57**(3): p. 149-151.
10. Konka, J., et al., *3D printing of hierarchical porous biomimetic hydroxyapatite scaffolds: Adding concavities to the convex filaments*. Acta Biomaterialia, 2021. **134**: p. 744-759.
11. Raja, N., et al., *Low-temperature fabrication of calcium deficient hydroxyapatite bone scaffold by optimization of 3D printing conditions*. Ceramics International, 2021. **47**(5): p. 7005-7016.

12. Tabard, L., et al., *Robocasting of highly porous ceramics scaffolds with hierarchized porosity*. Additive Manufacturing, 2021. **38**: p. 101776.
13. Simon, J.L., et al., *In vivo bone response to 3D periodic hydroxyapatite scaffolds assembled by direct ink writing*. Journal of Biomedical Materials Research Part A, 2007. **83A**(3): p. 747-758.
14. Yousefiasl, S., et al., *Bioactive 3D-printed chitosan-based scaffolds for personalized craniofacial bone tissue engineering*. Engineered Regeneration, 2023. **4**(1): p. 1-11.
15. Yeh, C.-L., et al., *Mechanical assessment and odontogenic behavior of a 3D-printed mesoporous calcium silicate/calcium sulfate/poly-ε-caprolactone composite scaffold*. Journal of the Formosan Medical Association, 2022. **121**(2): p. 510-518.
16. Xu, Z., et al., *3D printed MXene (Ti₂AlN)/polycaprolactone composite scaffolds for in situ maxillofacial bone defect repair*. Journal of Industrial and Engineering Chemistry, 2022. **114**: p. 536-548.1. Bandyopadhyay, A., S. Bose, and S. Das, *3D printing of biomaterials*. MRS Bulletin, 2015. **40**(2): p. 108-115.
17. Laubach, M., et al., *Clinical translation of a patient-specific scaffold-guided bone regeneration concept in four cases with large long bone defects*. Journal of Orthopaedic Translation, 2022. **34**: p. 73-84.
18. Phillips, M.R., et al., *A scoping review of operative and non-invasive management in the treatment of non-unions*. Injury, 2022.
19. Clarke, B., *Normal Bone Anatomy and Physiology*. Clinical Journal of the American Society of Nephrology, 2008: p. 9.
20. Olszta, M.J., et al., *Bone structure and formation: A new perspective*. Materials Science and Engineering: R: Reports, 2007. **58**(3): p. 77-116.
21. Murr, L.E., *Strategies for creating living, additively manufactured, open-cellular metal and alloy implants by promoting osseointegration, osteoinduction and vascularization: An overview*. Journal of Materials Science & Technology, 2019. **35**(2): p. 231-241.
22. Farid, S.B.H., *3 - Osteoinduction, osteoconduction, and osseointegration*, in *Bioceramics: For Materials Science and Engineering*, S.B.H. Farid, Editor. 2019, Woodhead Publishing. p. 77-96.
23. Su, A. and S.J. Al'Aref, *Chapter 1 - History of 3D Printing*, in *3D Printing Applications in Cardiovascular Medicine*, S.J. Al'Aref, et al., Editors. 2018, Academic Press: Boston. p. 1-10.
24. Bogala, M.R., *Three-dimensional (3D) printing of hydroxyapatite-based scaffolds: A review*. Bioprinting, 2022. **28**: p. e00244.
25. Lewis, J.A. and G.M. Gratson, *Direct writing in three dimensions*. Materials Today, 2004. **7**(7): p. 32-39.
26. Lewis, J.A., *Direct-write assembly of ceramics from colloidal inks*. Current Opinion in Solid State and Materials Science, 2002. **6**(3): p. 245-250.
27. Smay, J.E., et al., *Directed Colloidal Assembly of Linear and Annular Lead Zirconate Titanate Arrays*. Journal of the American Ceramic Society, 2004. **87**(2): p. 293-295.

28. Smay, J.E., J. Cesarano, and J.A. Lewis, *Colloidal Inks for Directed Assembly of 3-D Periodic Structures*. Langmuir, 2002. **18**(14): p. 5429-5437.
29. Smay, J.E., et al., *Directed Colloidal Assembly of 3D Periodic Structures*. Advanced Materials, 2002. **14**(18): p. 1279-1283.
30. Lewis, J.A., et al., *Direct Ink Writing of Three-Dimensional Ceramic Structures*. Journal of the American Ceramic Society, 2006. **89**(12): p. 3599-3609.
31. Alsharif, J.M.A., *Physical Dispersion of Nanocarbons in Composites - A Review*. 2017. **79**: p. 5.
32. Michna, S., W. Wu, and J.A. Lewis, *Concentrated hydroxyapatite inks for direct-write assembly of 3-D periodic scaffolds*. Biomaterials, 2005. **26**(28): p. 5632-5639.
33. Rehman, Z., et al., *Experimental study on the rheological behavior of tetrafluoroethane (R-134a) hydrate slurry*. Chemical Engineering Communications, 2018. **205**(6): p. 822-832.
34. Azahari, M.S.M., et al., *Acoustic properties of polymer foam composites blended with different percentage loadings of natural fiber*. IOP Conference Series: Materials Science and Engineering, 2017. **244**(1): p. 012009.
35. Hartatiek, et al., *Physical and mechanical properties of hydroxyapatite/polyethylene glycol nanocomposites*. Materials Today: Proceedings, 2021. **44**: p. 3263-3267.

VITA

David Jenkins

Candidate for the Degree of

Master of Science

Thesis: CHARACTERIZING POROSITY FOR 3D PRINTED HYDROXYAPATITE
SCAFFOLDS OF VARYING DENSITY AND COMPOSITION

Major Field: Materials Science and Engineering

Biographical:

Education:

Completed the requirements for the Master of Science in Materials Science and Engineering at Oklahoma State University, Stillwater, Oklahoma in December, 2022.

Completed the requirements for the Bachelor of Science in Geology at Texas A&M University, College Station, Texas in 2014.

Academic Employment:

- Research Assistant (January 2021-December 2022)
- Teaching Assistant (January 2021-December 2022)

Experience:

- PPE Manufacturing (March 2020 – December 2020)
- Installation Technician (November 2017 – December 2022)
- Patient Transporter (November 2016 – February 2017)
- Exploration Geologist Intern (May 2015 – August 2015)